BRNO UNIVERSITY OF TECHNOLOGY

VYSOKÉ UČENÍ TECHNICKÉ V BRNĚ

CENTRAL EUROPEAN INSTITUTE OF TECHNOLOGY BUT

STŘEDOEVROPSKÝ TECHNOLOGICKÝ INSTITUT VUT

IN VIVO APPLICATION OF HOLOGRAPHIC ENDOSCOPY

IN VIVO APLIKACE HOLOGRAFICKÉ ENDOSKOPIE

DOCTORAL THESIS TOPIC

DIZERTAČNÍ PRÁCE - POJEDNÁNÍ

AUTHOR

AUTOR PRÁCE

Mgr. Tereza Tučková

SUPERVISOR

ŠKOLITEL

Ing. Hana Uhlířová, Ph.D.

BRNO 2022

Abstract

The progress in understanding of complex brain function is conditioned by the ability to optically access any chosen structure and area in the living brain with minimal tissue damage and with sub-cellular resolution.

The progress in accessing deeper into the light-scattering tissue stands nowadays largely on the development of optical endoscopic probes such as microendoscopes with incorporated graded index (GRIN) lenses and fibre-optic bundles. Due to recent advancements in holographic light shaping methodology, using multimode optical fibres (MMF) as imaging elements has become promising for high resolution imaging deep in the tissue. In comparison to GRIN-based endoscopes and fibre bundles endoscopes, MMFs provide the highest ratio of image resolution and probe thickness causing minimal tissue damage.

This thesis first provides an overview of the current state-of-the-art *in vivo* deep brain imaging technology, multi-mode fibre-based endoscopy and its principles to introduce the related technology. The main technological focus of the thesis stands on using a digital micro-mirror device (DMD) to modulate light through the MMF probes. This enables fast raster scanning of the fluorescent sample at the imaging plane of the fibre distal facet. An optical setup exploiting this principle has been built, its imaging properties carefully evaluated, and high stability reached. Its imaging abilities have been demonstrated on 2D and 3D fluorescent phantom samples.

Consequently, we have developed an image post-processing procedure to enhance the detected image and reach the full diffraction-limited resolution potential. Using algorithms, one based on a regularised iterative inversion and second on regularised direct pseudo-inversion, lead to enhancement of the image contrast and resolution.

Further, we used genetically modified mice to move towards *ex vivo* and *in vivo* imaging. Suitable mouse models were identified and its *ex vivo* brain imaging showed that the images suffer from strong background fluorescent signal from out-of-focus planes. Therefore, further work focused on technological development for light attenuation based on the confocal principle.

An optical setup for confocal “pinhole” filtration has been built using a custom-made probe consisting of graded-index MMF spliced at the tip of the step-index MMF and a second DMD. The fluorescent signal collected by the GRIN-SI-MMF was filtered in the probe far field where for every scanning focal point it forms an annular ring. This ring-signal, and thus also the out-of-focus signal, was then separated using a mask on DMD2. On a set of experiments using phantom sample of fluorescent microspheres and fixed brain tissue it has been demonstrated that this confocal filtering leads to attenuation of the background signal, the signal from the out-of-focus planes thus enhancing the images contrast and resolution. This principle of confocal filtering in the holographic endoscope has been also demonstrated using a novel side-view MMF probe.

This work shows a piece of a puzzle in a long-term complex development of an optimal tool for deep-tissue and high-resolution imaging. The MMF-based holographic endoscope has been advanced to routine imaging of biological tissue in range of hours with the feature of out-of-focus light attenuation. The endoscope has been tested on imaging of phantom samples as well as fixed mouse brain slices and *in vivo* vasculature down to depth of 5 mm.

Keywords

Holographic endoscopy, microendoscopy, optical fibre, multimode fibre, light modulator, digital micro-mirror device, transmission matrix, fluorescence imaging, computation image enhancement, mouse model, genotypization, tissue preparation, *ex vivo* imaging, confocal imaging, out-of-focus light suppression, *in vivo* imaging

Abstrakt

Pokrok v porozumění komplexním mozkovým funkcím závisí na schopnosti opticky dosáhnout jakékoli vybrané struktury a oblasti živého mozku se subbuněčným rozlišením při minimálním poškození tkáně.

Zpřístupňování hlubších oblastí tkání rozptylujících světlo je v současnosti umožněno zejména vývojem optických endoskopických sond, například mikroendoskopy s gradientními čočkami (GRIN) a svazky optických vláken. Pokrok v metodách holografické modulace světla dosažený v poslední době přinesl jako další nadějný směr pro zobrazování s vysokým rozlišením hluboko ve tkáních použití vícevidových optických vláken (MMF) jako zobrazovacích prvků. Ve srovnání s endoskopy založenými na GRIN čočkách a svazcích optických vláken poskytují MMF nejvyšší poměr rozlišení obrazu ku tloušťce sondy a způsobují minimální poškození tkáně.

Úvodní část práce poskytuje přehled o nejmodernějších technologiích hloubkového zobrazování mozku *in vivo*, vícevidové vláknové endoskopii a jejích principech s cílem představit související technologii. Hlavním technologickým zaměřením práce je použití digitálního mikrozrcátkového zařízení (DMD) k modulaci světla, šířící se MMF sondou. To umožňuje rychlé rastrování fluorescenčního vzorku v zobrazovací rovině za distální hranou vlákna. Byla sestrojena optická sestava využívající tohoto principu, bylo dosaženo vysoké stability a byly pečlivě vyhodnoceny zobrazovací vlastnosti. Ty byly demonstrovány na 2D a 3D fluorescenčních fantomových vzorcích.

Dále jsme vyvinuli metodu zpracování obrazu, zlepšující jeho kvalitu a umožňující dosáhnout plného potenciálu difrakčně omezeného rozlišení. Použití algoritmů využívajících regularizované iterativní inverze, případně regularizované přímé pseudoinverze, zvyšuje kontrast a rozlišení obrazu.

Další cestou k *ex vivo* a *in vivo* zobrazování bylo použití geneticky modifikované myši. Identifikovali jsme vhodné myší modely a *ex vivo* zobrazování mozku ukázalo, že snímky trpí silným fluorescenčním signálem pozadí z oblastí mimo ohniskovou rovinu. Proto se další práce zaměřila na vývoj technologie útlumu světla založené na konfokálním principu.

Byla sestrojena optická sestava pro konfokální filtraci "dírkovou clonkou" s použitím speciální sondy složené z MMF s odstupňovaným indexem lomu spojeného s MMF se skokovým indexem, a druhého DMD. Během zobrazování byl fluorescenční signál shromážděný GRIN-SI-MMF sondou filtrován ve vzdáleném poli sondy, kde se pro každý skenovací ohniskový bod vytváří prstenec. Prstencovitý signál se pak oddělí pomocí masky na DMD2, čímž se také oddělí signál pocházející z ohniska od signálu vznikajícího mimo ohnisko. Na experimentech s použitím fantomového vzorku fluorescenčních mikrokuliček i fixované mozkové tkáně bylo prokázáno, že toto konfokální filtrování vede k zeslabení signálu pozadí, tedy signálu z mimoohniskových rovin, čímž se zvyšuje kontrast a rozlišení snímků. Tento princip konfokální filtrace v holografickém endoskopu byl rovněž demonstrován pomocí nové MMF sondy s bočním zobrazováním.

Práce ukazuje jen kousek skládačky dlouhodobého komplexní vývoje optimálního nástroje pro hloubkové tkáňové zobrazování s vysokým rozlišením. Holografický endoskop využívající MMF byl zdokonalen tak, že může sloužit k rutinnímu několikahodinovému zobrazování biologických tkání s možností útlumu světla pocházejícího mimo ohniskovou rovinu. Endoskop byl testován při zobrazování fantomových vzorků i fixovaných plátků myšího mozku a *in vivo* cév až do hloubky 5 mm.

Klíčová slova

Holografická endoskopie, mikroendoskopie, optické vlákno, vícevidové vlákno, modulátor světla, digitální mikro-zrcátkové zařízení, přenosová matice, fluorescenční zobrazování, výpočetní vylepšení obrazu, myší modely, genotypizace, příprava vzorku tkáně, zobrazování *ex vivo*, konfokální zobrazování, potlačení světla z oblastí mimo ohniskovou rovinu, zobrazování *in vivo*

Acknowledgment

I would like to express my sincere gratitude towards my supervisor Dr. Hana Uhlířová for introducing me to the world of neuroscience and microscopy, for her patient, thorough and forthcoming supervision and guidance through my whole Ph.D. study. She has been a great mentor to me, always ready and keen to discuss various scientific problems. I am grateful for all the advancement, professional and personal, I have made because of her.
My sincere gratitude also belongs to prof. Tomáš Čižmár for the opportunity to be part of the project and research team. I am glad he was the thought-leader of the project and that he was constantly creating a nurturing environment for the team to function. I am grateful to prof. Pavel Zemánek for allowing the project to nest at the Institute, for taking care of the environment and everything necessary for the research. I would like to thank also my colleagues – Dr. Martin Šiler, Dr. Petr Jákl, Dr. Sergey Tuartev, Dr. Dirk Boonzajer Flaes – for sharing their experience and wisdom, and to MVDr. Petra Ondráčková who guided me through the world of laboratory animals, gave me courage and with her enthusiasm motivated me to advance further.
I will always remember and be thankful my closest colleagues - Tom Pikálek and Mirek Stibůrek – whose support, friendship and attitude always pushed me a step further.
I am also especially thankful to prof. Radim Chmelík, whose research group I used to be a part of, for all the care and support, for scientific discussions and advice and for allowing us to use the group's lab.
My eternal thanks go to my husband Marek for immediate and intense support and to my whole family for always being there for me.
I am grateful to CEITEC BUT and ISI ASCR for supporting my studies, courses, conferences and professional growth.

The European Regional Development Fund-Project Holographic endoscopy for in vivo applications (CZ.02.1.01/ 0.0/ 0.0/ 15_003/0000476, LO1212); European Commission (101016787, CZ.1.05/ 2.1.00/ 01.0017) and CAS (L01212, CZ.1.05/2.1.00/01.0017, RVO:68081731 are gratefully acknowledged for the support of this work.

I declare that I have written this thesis entitled *In vivo application of holographic endoscopy* independently, under the guidance of the supervisor, Ing. Hana Uhlířová, Ph.D., and using the technical literature and other sources of information, all adequately cited in the thesis, with a detailed list of references provided at the end of the thesis.

Mgr. Tereza Tučková

Contents

1. Introduction

Since the origin, there has been a strong desire to understand what is the essence of humankind. What is the drive that gives people desires, ideas, and cravings for the understanding of life and the universe? Already in Ancient Egypt four thousand years ago, the human body was studied in morphology and physiology. However, due to the limited opportunities in those times, it was feasible only postmortem and by observation of the human behavior. Therefore, to explain and describe the very principle of brain function was impossible. It was not until the blossoming of science at the end of the 19th century before a significant progression in the field of neuroscience happened. The advancement in microscopy, labelling of the tissue, imaging using X-rays and electroencephalography enabled to reveal the structure of the brain and indirectly record its activity for the first time.

In the second half of the 20th century, the rapid progress in molecular biology, biochemical processes, electrophysiology, and computational methods enabled to study connectivity between single neurons. The neuronal study offers an expansion of our understanding of social evolution as well as cognitive and behavioral development or the process of making decisions. Due to the ever increasing precision of technology, a rapidly growing number of patients became diagnosed with neurodegenerative diseases such as Alzheimer's and Parkinson´s as well as with epilepsy, migraine strokes, and others. This motivates an urgent need for understanding of brain mechanism and its functional connectivity. Most of these pathologies are difficult to study *ex vivo*, therefore the progress of neurological/neurobiological research has greatly depended on technology enabling to exploit animal models. Among all animal models, mouse became the most popular because of its small size, fast reproduction cycle, yet up to ~85% conformity of protein-coding regions with the human [1].

The current non-invasive methods, which can also be used in humans, such as computation tomography (CT), positron emission tomography (PET), nuclear magnetic resonance (NMR), or ultrasound enable to investigate the structural changes or in the case of functional magnetic resonance imaging (fMRI) functional processes and connectivity in the brain. These techniques yield macroscopic information from the whole brain due to their high penetration, however with limited resolution sufficient for distinguishing of individual cells, as summarized in Fig. 1.1.

Very soon it became clear that understanding the cause and early pathogenesis of neuronal diseases requires studying the underlying structural and functional changes on a cellular and sub-cellular level.

Current *in vivo* neuroscience research meets these needs mainly via optical microscopy providing high-resolution structural and functional imaging. However, optical methods suffer a fundamental trade-off between the penetration depth and resolution (Fig.1.1). To overcome this depth limitation, optical probes, such as endoscopes have to be used.

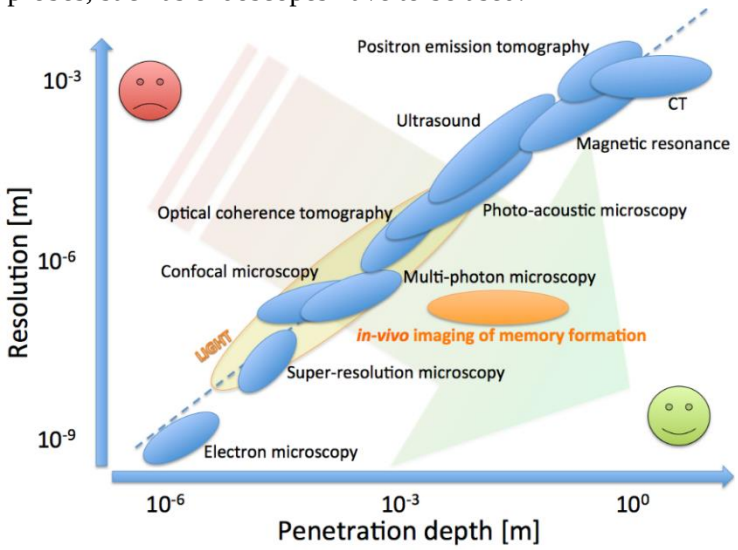

Figure 1.1: The trade-off between resolution and penetration depth for methods of biomedical and biological imaging. Reprinted from [2].

1.1 Current state-of-the-art optical methods for *in vivo* imaging in neuroscience

Light provides exquisite sensitivity to capture brain structure and function via intrinsic changes in absorption, scattering, or extrinsic contrast. Technological advancements in light laser scanning microscopy, digital acquisition, and progress in fluorescence labelling methods in the last two decades have enabled monitoring the activity of thousands of cells with their interactions within brain circuits with sub-cellular resolution [3].

1.1.1 Limits of optical imaging

One of the main challenges for optical technology is to acquire high-resolution images from deep within the brain *in vivo*. The optical methods presented in this work use for signal excitation scanning with a laser beam focused into a focal point. The quality of obtained resolution is intrinsically linked to the numerical aperture of the optical system and the wavelength of the illumination laser, and the refractive index of the imaging medium or sample. The optimal resolution of the imaging system is limited only by diffraction and can be described by the Rayleigh resolution criterion in equation

$$R = 0.61\frac{\lambda}{\mathrm{NA}}, \tag{1.1}$$

where λ is the wavelength of the illumination beam and NA is the numerical aperture of the objective defined as $n \cdot \sin\theta$, where θ is an acceptance angle measured from the optical axis and n refractive index of the medium. The resolution limit along the optical axis can be described by the axial resolution of the focused point, also defined with Rayleigh criterion [4] in equation

$$R = \frac{2\lambda}{\mathrm{NA}^2}. \tag{1.2}$$

The depth to which the light can penetrate is affected by the optical properties of the sample. Living tissue is an optically turbid heterogeneous medium with a complex variety in the refractive index, absorption and high scattering properties resulting in attenuation of the propagated light where scattering being much more prominent. For the brain tissue, the scattering length (empirically measured), describing the distance over which scattering reduces light intensity by a factor of 1/*e*, is, is in the range ~20-100 μm for visible light [6] and ~220 μm for near-infra red light (NIR) [7, 8]. Imaging at depths of ~500 μm below the brain surface suffers from multiple scattering events limiting the achievable contrast. These fundamental limits motivate a massive effort to develop imaging modalities robust to light scattering. The following sections offer a description of some of the most successful methods.

1.1.2 Confocal microscopy

Confocal microscopy exploits an optical process involving a single photon absorption followed by the emission of a single fluorescence photon of a longer wavelength. It is therefore a linear optical technique [9, 5]. Confocal microscopy enables the imaging of thick samples. It effectively suppresses the light from planes other than the imaging one (the out-of-focus light) [10, 11, 12]. For the illumination, it uses a focused laser beam scanned within the sample across the focal plane [12, 13, 14]. Its essential part is the pinhole acting as a spatial filter at the conjugate image plane positioned in front of the sensitive detector a photomultiplier tubes (PMT) rejecting the photons emitted from out-of-focus areas or scattered photons. The blocked signal does not contribute to the image which dramatically improves contrast and the resolution [12, 13, 14]. With confocal microscopy, the lateral and axial resolutions can reach values around 180 nm and 500 nm, respectively [15, 16]. With the increasing imaging depth, the contrast of the image decreases very quickly. Stronger illumination is needed with a decreasing size of the pinhole. The whole illuminated volume suffers therefore by photobleaching and phototoxicity as the tissue is repeatedly illuminated. [17].

1.1.3 Multiphoton microscopy

Multiphoton microscopy is currently a well-established microscopy technique for deep imaging within the intact brain or bulk tissue. It is a nonlinear technique involving multiple photons´ absorption (mostly with the same energy or different energies [18]) using femtosecond pulsed lasers, followed by the emission of a fluorescent photon. The used excitation wavelengths are in the NIR range, which are less scattered in biological tissue leading to a greater penetration depth compared to visible light [19, 20].

The two-photon absorption depends quadratically on the incident light intensity [21]. The excitation is localized only in the small focal volume centred at the focal plane. The two-photon microscopy using NIR wavelengths enables to image to the depth of ~750 μm below the brain surface [5, 19, 22]. An optical parametric oscillator (OPO) can extend wavelength of some lasers thus offering a tuneable wavelength up to ~1300 nm. This enables to reach imaging depth of 1.6 mm at 1280 nm wavelength [23]. The three-photon microscopy uses wavelengths around ~1300 nm and longer enabling greater penetration depths for imaging. The dependence of the probability of photons absorption on the incident light intensity is cubic. The three-photon excitation reduces the out-of-focus signal stronger than two-photon excitation. The three-photon microscopy can achieve high-resolution *in vivo* imaging at depth from ~1.100mm [24] up to ~1.600 mm [25, 26].

The multi-photon microscopy is currently the primary choice for optical far-field microscopy of brain *in vivo*. However, many structures important for higher brain functions (e.g. cognition and learning) lie below the achievable depth limit of multi-photon microscopy. One of the potential solutions would simply surgically removing the part of the tissue lying above the region of interest [27]. This approach however is very invasive and interferes with the physiology and function of the brain [28].

1.1.4 Microendoscopy

Microendoscopes are thin optical, usually rigid probes of 350-2000 μm in diameter guiding the light to the hardly accessible areas of the tissue enabling deep tissue imaging, also *in vivo*. Microendoscopes primarily act as optical relays and several imaging techniques have been accomplished deep inside the brain: two-photon microscopy [29, 62], epifluorescence [30, 31], confocal [32, 33, 34], light-sheet microscopy [35] and super-resolution imaging [36]. Few relevant types of micro-endoscopes are shortly introduced in the following chapters.

Endoscopy using GRIN lenses

One prominent type of micro-endoscopes is based on a gradient index (GRIN) miniature rod-like lenses with a parabolic profile of the refractive index [37] characterized by their length and numerical aperture NA [40]. They are formed by up to three GRIN lenses (singlet/doublet/triplet, see Fig. 1.2) delivering illumination into the brain tissue and relaying the emitted photons of fluorescence signal from structure in the tissue to microscope objective [38, 40].

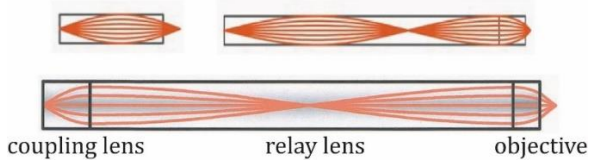

Figure 1.2: Different types of GRIN probes – singlet, doublet and triplet, formed by an objective lens, a relay lens, and a coupling lens. Reprinted from [38].

The GRIN microendoscopes are commercially available with NA up to ~0.8 and diameters from 0.35 to 2.8 mm. Using GRIN microendoscopes of 1 mm in diameter one can reach lateral and axial resolution for 2-photon imaging ~0.85 μm and ~7.4 μm [42] or for 3-photon imaging resolution of ~1 μm and ~9.5 μm [43]. The urgent need for microendoscope minimalization has led to the use of the probe of 350 μm in diameter with assembled aspheric lenses and with 2-photon imaging was reached a resolution under 1 μm [39] successfully implemented in high-resolution *in vivo* laser-scanning imaging in animals and humans [39, 41, 44, 45].

The resolution of the system is limited by optical aberrations within the endoscope probes [46]. Adaptive optics can provide correction of the aberrations [47, 48, 49, 50]. The GRIN probes are also used in miniaturized head-fixed microendoscopes for imaging in freely behaving animals using multi-photon [51, 52, 53, 54] excitation. GRIN microendoscopes are one of the significant tools for *in vivo* imaging of deep brain. However, they require aspiration of part of the tissue which can compromise the physiological function of the surrounding tissue or the tissue under study [55].

Endoscopy using optical fibre bundles

Fibre bundles (~80-300 μm up to few millimetres in diameter) are a flexible alternative to rigid GRIN probes constructed from thousands of thin single-mode optical fibres (SMF) of core diameters ~3-7 μm with a relatively low NA (~0.22). Each of them can transfer only a single spatial mode of light, one image pixel value at a time. Only packed together they obtain an image information (Fig. 1.3) from deep region of the sample. However, the detected light collection efficiency is low [57] and the images suffer from pixelation artefact leading to low lateral resolution [56, 57].

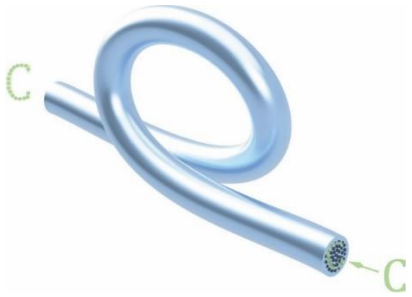

Figure 1.3: Transmission of the image in the fibre bundle consisting of many spatially separated cores. The light from the letter C is propagating only through the spatially separated cores placed within the cladding, all packed within one probe.

A magnifying optics (a set of microlenses [58] or a GRIN lens [59]) attached to the end of the bundle on the sample side can increase the resolution or the implementation of several techniques (e.g. confocal microscopy [33, 60]). They insertion requires surgical removal of a significant volume of brain tissue, compromising the physiology [63].

Endoscopy using Step-Index (SI) Multi-Mode optical fibres (MMFs)

The tissue removal for deep *in vivo* imaging can lead to mechanical lesions of the tissue compromising the physiology of neuronal networks and the behaviour of the animal [64, 65]. A promising probe of a much smaller diameter providing sub-cellular resolution can be a multimode optical fibre (MMF), as summarized in Fig. 1.4. Step-index MMFs consist of a higher refractive-index core of diameter of ~10-1500 μm and lower refractive-index cladding with outer diameter of ~110 - 1550 μm and the NA reaching values up to ~0.9 [72]. Step-index MMFs are comprised of a glass core surrounded by a glass cladding with a lower refractive index forming a closed cylindrical refractive index boundary. It entraps and guides the light by total internal reflection. Coherent light is coupled into many propagating modes (10 000 modes up to hundreds of thousands [66]) resulting in MMF having a large information capacity. The whole NA of the MMF can be utilized. The image resolution is fundamentally limited only by diffraction [67, 68, 61, 69, 70, 71]. MMFs have the rays entering fibre input facet at an incident angle within the cone defined by the acceptance (aperture) angle θ_a are coupled and propagate through the fibre in the form of propagating modes. The acceptance angle, measured from the optical axis, can be described as

$$\theta_a = \mathrm{asin}NA \tag{1.3}$$

where NA is the numerical aperture of the fibre [37]. The MMF acts like a complex medium in which the light is subject to the process of multiple scrambling. After propagation the light outcome in a

random speckle pattern. The development of digital holography methods allows modulating the coherent light through highly scattering media and enables creation of the focus and imaging through MMF [68, 70, 73, 74, 75, 76]. The wavefront modulation technique has been exploited in combination with approaches including among others ([76, 77, 78, 79, 80, 81]) the concept of transformation matrix (TM) [75, 82].

Among the described endoscopic probes, MMFs provide the highest resolution to probe thickness ratio (see Fig. 1.4). Thus, the MMF can serve as an atraumatic probe and can be inserted deep into the brain tissue. The probes up to ~200 μm in diameter do not require surgical removal of the tissue. The MMFs with a core diameter of ~50 μm and ~0.22 NA have been mostly used for *in vivo* imaging [71, 83, 84] down to 4 mm under the brain surface with lateral resolution of ~1.2 μm [71].

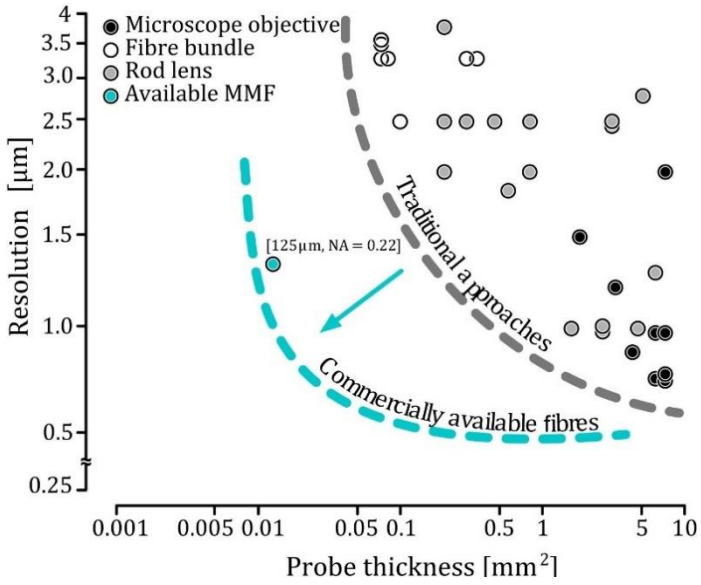

Figure 1.4: The relation between probe thickness and its resolution across the commercially available microendoscopes. Reprinted from [83].

1.2 Summary of the thesis

This Ph.D. work focuses on the development of imaging methods applied via the MMF-based endoscope for deep *in vivo* brain imaging.

The first part presents the current state-of-the-art optical techniques, which have also been used in this work. In the next part, the basics and principles of holographic endoscopy are introduced.

In the Result section, I first described the basic setup replicated in Brno according to the published work of the research group [71]. The imaging performance is demonstrated on fluorescent 2D and 3D model samples such as fluorescent micro-spheres and the USAF target. To enhance the image quality, two computational algorithms are introduced which enable to reconstruct the sample with increased contrast and resolution.

The collected knowledge has served as the starting point for building a setup of a new generation for *in vivo* brain studies in mouse models. Consecutively as the next step, Further, I present selected mice lines which represent the best available models for imaging along with their preparation and surgical procedures. Neuronal imaging of fixed brain slices revealed that despite sparse fluorescence expression high resolution imaging may be difficult due to the out-of-focus light imaged inherently in all one-photon excitation techniques.

This motivated our effort to implement one of the strategies for out-of-focus light attenuation. The last part of this thesis introduces a holographic endoscope which exploits a custom-designed probe spliced from two types of MMF for confocal filtering of the detected signal. The principle is demonstrated on both phantom samples as well as brain tissue.

1.3 Aims of the thesis

The following aims has been specified at the beginning of the PhD studies.

1. Holographic endoscopy through MMF

The first aim of the dissertation work is to build the multimode fibre-based holographic endoscope. The set-up should be designed according to the published work of the research group [103]. The set-up should be tested on model samples such as fluorescent beads and resolution targets. The performance of the setup imaging should be characterized with an appropriate metrics. Experience with this setup should serve as the starting point for building a setup of new generation for in vivo brain studies in mouse models.

2. Preparation for animal surgery

The second aim is establishing and testing of protocols for animal brain surgeries necessary for the endoscope fibre implantation. In the first step, the endoscopy will be carried out in acute experiments on anesthetized animals. In the next step, a protocol for chronic imaging in awake animals should be developed.

3. *In vivo* imaging and out-of-focus attenuation via MMF-based endoscopy

The third aim of the dissertation work comprises implementation of the endoscope setup as well as the developed animal preparation protocols in high resolution of deep brain structures and potentially functions *in vivo.* Suitable genetically modified mouse models have to be selected and the imaging of fluorescence deep in the tissue demonstrated. Imaging should be performed on anesthetized animals and potentially extended to awake head-fixed animals.

2. Holographic endoscopy based on MMFs

Since the MMF behaves like a complex turbid medium to use it as an imaging tool, it is necessary to characterize the light propagation. Using wavefront shaping, the scrambling of light in a MMF can be measured and corrected for. Then, it can be used to transmit and collect images similarly to scanning microscopy.

2.1 Light propagation through a multimode optical fibre

A step-index MMF (SI-MMF) is a cylindrical dielectric waveguide defined by two different constant refractive indices for the core (n_1) and the cladding (n_2). The common SI-MMF probes used for imaging have total diameter of 125-400 μm with core diameters of 50 - 200 μm [85]. Light coupled into the fibre core is defined by the acceptance (aperture) angle θ_a and the modes propagate by total reflection of the core to cladding interface. The acceptance angle is crucial, described by the relation in Eq. (1.3), with NA of the fibre defined by the refractive indicies of the core (n_1) and cladding (n_2) as $\mathrm{NA} = (n_1{}^2 - n_2{}^2)^{1/2}$. The light entering the fibre input facet at angles larger than θ_a can be refracted into the core, but the modes do not undergo total internal reflection. Depending on the coupling angle, each mode propagates through the fibre with a different trajectory along the core axis with a different phase velocity. At the output, modes meet in one plane with different phase shifts yielding a speckle pattern (Fig. 2.1), which is not suitable for fluorescent imaging.

Figure 2.1: Coherent light coupled to the MMF exits as a spackle pattern due to different phase velocities of different propagating modes.

Since the light propagation through the MMF is considered a deterministic and linear system [82, 86], it can be analytically described, and the phase shifts can be compensated for by modulation of the input wavefronts´ phase and amplitude using a linear operator the transmission matrix (TM) [82].

2.2 Transmission matrix

The transmission matrix (TM) describes the relation of the optical light field at the input facet of the MMF (a proximal facet to the DMD) and the output facet (distal facet to the DMD), providing linear transformation between them [82] containing phase and amplitude of the propagating light.

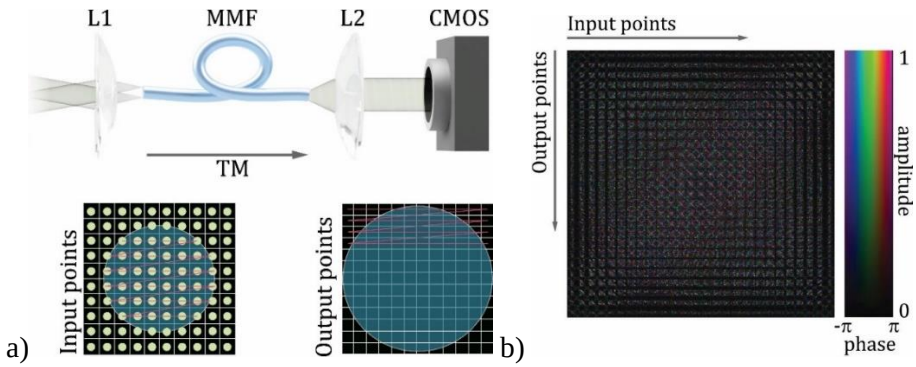

Figure 2.2: a) Orthogonal bases of input and output points used for TM measurement. The lens L1 focuses the beam scanned across the input facet of MMF in the form of input points during the TM measurement. The outcoming light is collimated with lens L2 onto chip of the camera (CMOS). Illustration of the bases of the input points across the input fibre facet and the grid of the pixels of the camera creating an orthogonal base of output points (bottom panel). b) The example segment of measured transmission matrix with complex coefficients [70]. Values of amplitudes and phases of each output point for all single input points are written into each row.

The TM is considered unitary [70]. It is measured by decomposing both complex fields into orthogonal bases of input and output modes. We measure the TM using localized input points (or plane waves [68, 70]) on the facet and output points from the facet imaged into corresponding pixels on a camera (Fig. 2.2). Each output point (E_m^{out}) is then defined as

$$E_m^{out} = \sum_n t_{mn} E_n^{in}, \tag{2.3}$$

where t_{mn} are complex coefficients of the TM and E_n^{in} is the complex amplitude of the optical field in the n^{th} input point [91, 72, 82]. An example of an experimentally measured transmission matrix is shown in Fig. 2.2b).

2.3 Light modulation using a digital micro-mirror device (DMD)

Wavefront manipulation can be achieved using two of the most commonly used modulators: liquid crystal-based spatial light modulator (LC-SLM) or an optical microelectromechanical system MEMS-based SLM, e.g. digital micro-mirror device (DMD). In our work we use a DMD. DMDs are pure high-resolution amplitude binary modulators, which can be used effectively for phase modulation using diffraction of light [87], typically in an off-axis regime. The DMD chip consists of hundreds of thousands of micro-mirrors with the state "on" (1) or "off" (0) corresponding to a single pixel in the displayed image. The resolution of commercially available DMD climbed up to 2048x1152 pixels [88, 89, 90, 92]. The DMD has been often used in a regime of phase-only modulation and thus the modulation of light in created focus reaches efficiency of 75% [69, 87] or recently for a complex modulation of the wavefront with increased efficiency up to 96% [93]. The DMDs operate at a frame rate, up to 22 kHz, which is one of the main reasons the DMDs are the first choice for biological imaging applications where temporal resolution is essential [94, 95].

Figure 2.3 schematically describes holographic wavefront modulation, where the DMD chip acts as a diffractive grating providing a binary computer-generated hologram (CGH). Such hologram diffracts light into diffraction orders given by the hologram spatial frequency. For calibration, a set of single-frequency diffraction grating in DMD plane is used by 4f system creating input points at the input fibre facet.

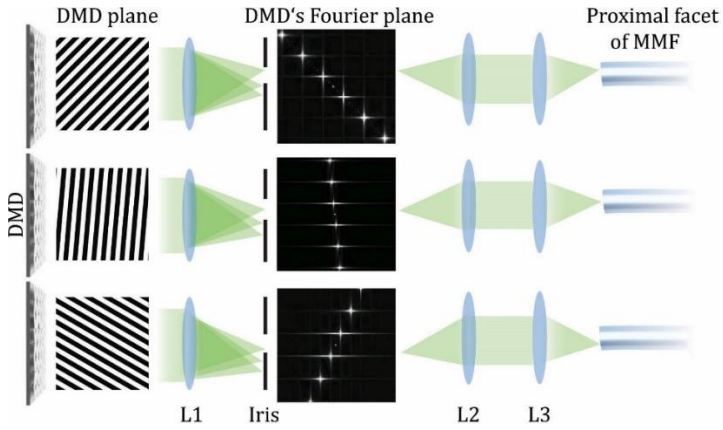

Figure 2.3: A simplified principle of the light diffraction of a single-spatial frequency hologram. The light diffracts on the grating displayed on the DMD into diffraction orders which are imaged by the lens L1 into the DMD´s Fourier plane. The iris diaphragm selected 1st order here. Lenses L2 and L3 image the Fourier plane on the proximal (input) facet of the MMF. Changing the diffraction grating results in the change the position of the focused point at the input facet.

2.4 Optical setup

The optical setup in Figure 2.4 uses a single-frequency coherent laser of 532 nm wavelength The laser beam going through an isolator and a half-wave plate (H1) and a polarization beamsplitter (PBS) (controlling the total power in the system) is split on a polarization beam splitter (PBSW) into signal and reference beams aligned into the single-mode polarization-maintaining optical fibre (SMF1 and

SMF2) by combination of H3, H4 and lenses L1, L2. The isolator was implemented in order to isolate unwanted polarization. The wavefront from the signal beam is then diffracted by the DMD using only the micromirrors in the "on" state (+12°). An iris to select the 1st diffraction order is placed into the Fourier plane of the DMD. The light further travels through lenses and is focused (L6) onto the input facet. After propagation through the MMF the speckle pattern is imaged on a CMOS camera. Then the calibration is performed. A reference beam is sent onto the camera and the TM is measured.
At the beginning of each experiment, or after the replacement of the fibre, it is necessary to calibrate the system, i.e. measure a new TM with the MMF immersed into a medium with the refractive index matching the refractive index of the sample.

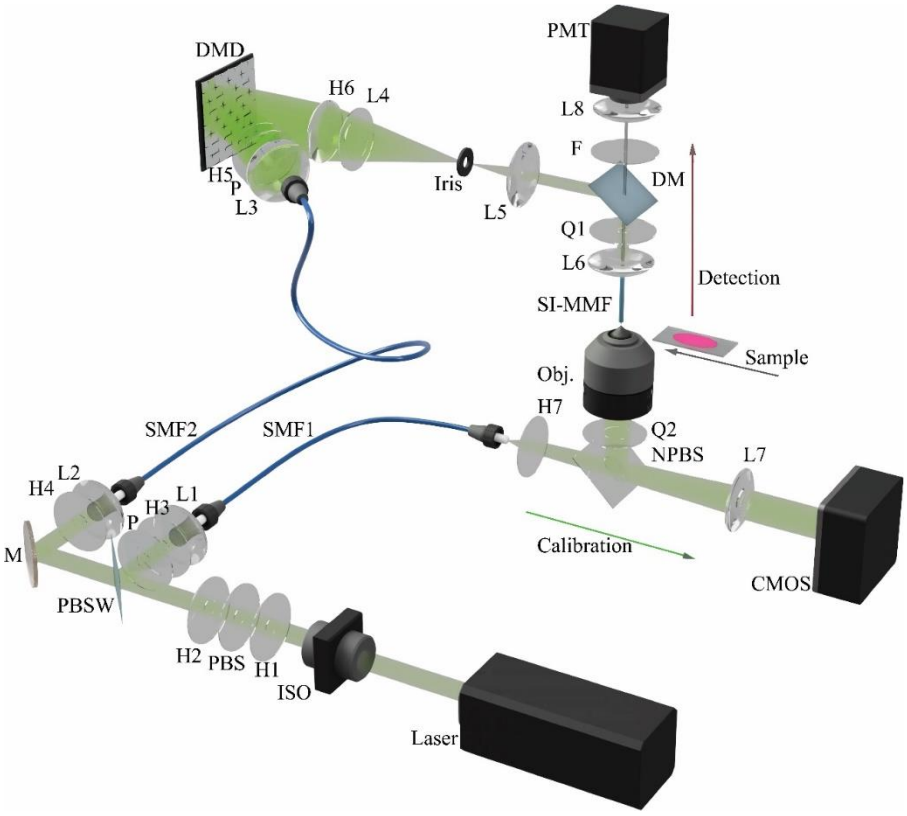

Figure 2.4: Experimental setup with the calibration module and detection path: **Laser:** Coherent Verdi G-Series 532nm; **M:** Mirror BB1-E01, Thorlabs. **L1, 2**: Lens C240TME-A, Thorlabs. **L3, 5, 8**: Achromatic Doublet AC254-075-A-ML, Thorlabs. **L4, 7**: Achromatic Doublet AC254-150-A-ML, Thorlabs. **L5:** Achromatic Doublet AC254-075-A, Thorlabs. **L6**: Achromatic Doublet, AC254-080-A-ML, Thorlabs. **H1-H7**: Multi-Order Half-Wave Plate WPMH10M-532, Thorlabs. **Q1,2:** Multi-Order Quarter-Wave Plate, WPMQ10M, Thorlabs. **PBS:** Polarizing Beam Splitter, CCM1-PBS25-532/M, Thorlabs. **PBSW:** Polarizing Plate Beamsplitter PBSW-532, Thorlabs. **P:** Linear polarizer LPVISE 100-A, Thorlabs. **DM:** Dichroic mirror, Chroma, **F:** Filter ET525/50, Semrock. **NPB:** Non-polarizing Beamsplitter Cube BS016, 50:50, Thorlabs. **SMF1:** single-mode optical fiber maintaining polarization, PM SMF, SQS Vláknová Optika, PM460-HP. **SMF2**: Single Mode Fibre P3-488PM-FC-2, Thorlabs. **ISO**: Isolator Tornos Serie 500-1030nm (04-532-00012). **DMD**: Digital micro-mirror device V-7001 (DLP 7000, Texas Instruments), ViALUX. **Iris**: Iris diaphragm SM1D12C, Thorlabs. **SI-MMF**: Step-Index Multimode Fibre FG050LGA, Thorlabs. **Obj.:** Objective, Olympus 20x, NA = 0.22. **CMOS**: Camera Ace acA640-750um, Basler. **PMT**: Photomultiplier Tube PMT2101/M, Thorlabs.

For the measurement of the TM the input modes are selected based on intensity transmitted through the fibre which is recorded on the camera (Fig. 2.5). The output points are selected within the grid of 224x224 pxls^2. As a result, we measure the TM between ~4100 input and ~50 200 output points in the calibration process.

2.5 Calibration procedure

The calibration procedure is performed by phase-shifting interferometry. The focal plane for the calibration – the distance of the MMF facet, is for our type of MMF typically set to ~30 μm. There the measurement of the output points phase modulation uses interference with external reference beam, both imaged on the camera. Using the principle of phase-shifting interferometry, we modulate and measure each phase of every input point and alter mutual shifts of the outcoming light from the fibre and the reference light at the output spot (pixel) on the camera and compensate for them. Thus, we can define how to change phase and amplitude of the input point to reach a maximal constructive interference in a particular output point (pixel) on the camera.

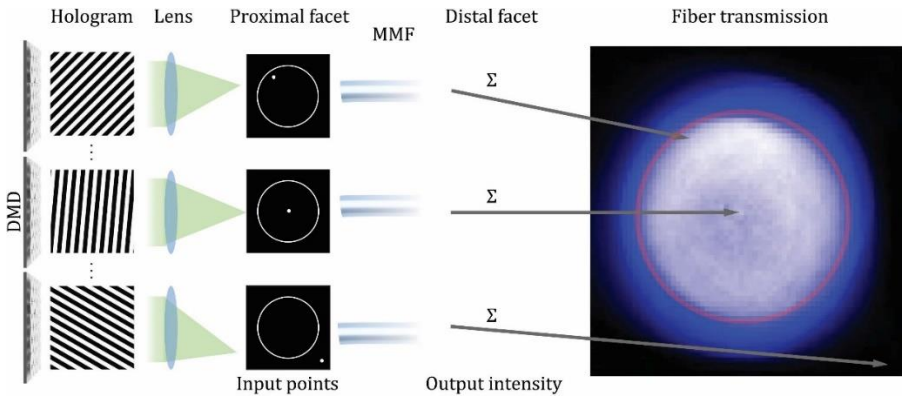

Figure 2.5: Input and output points are selected based on the sum of the total intensity of the light transmitted through the fibre.

Firstly, the input points coupled into the MMF and used for the TM measurement are selected based on intensity transmitted through the fibre which is recorded on the camera and defined within a created "mask" (Fig. 2.6, red ring).

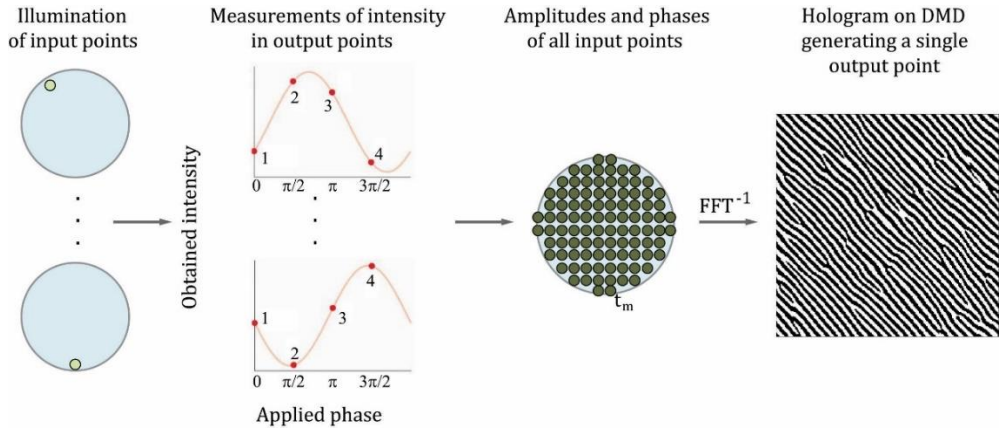

Figure 2.6: Generation of a focal spot at the output of the fibre. For every input point, amplitude and phase shift in the corresponding output point is measured. This input field of complex amplitudes t is inverse Fourier transformed and binarized to obtain the hologram, which is then displayed on the DMD. The wavefront modulated by this hologram forms a focal spot at plane at chosen distance from the output facet.

The output field at the distal end of the MMF is imaged on the camera, where the output points are defined in a grid with inscribed circle (output field) of the size 224×224 pxl². Each pixel in this grid is assigned to each output point. Then, we measure the phase shift of the light in every output point for every single input point using phase-shifting interferometry. The phase of input points is shifted by $\pi/2$ in eight steps ($\alpha = 0, \pi/2\,, \pi, 3\pi/2$) sampling the intensity cycle two times (as illustrated in Fig. 2.7). The input points are measured sequentially, while output modes are measured simultaneously on the camera. The phase shift φ is calculated from measured intensity multiplied with the corresponding phasor for each step and summed over all steps. The amplitude is calculated as a measured amplitude

from the sinus from the Fig. 2.7. The values of each output point measured and calculated for all single input points are written into each row of the TM.
The last step is to create the holograms projected on the DMD generating output focal points. A line of the TM corresponding to the appropriate output mode is selected, reshaped into the dimensions of input modes and an inverse Fourier transform is applied. This complex matrix is then binarized and the result is displayed on the DMD (Fig. 2.6). Sequential formation of focal points in a square grid mimics scanning of a classical scanning microscope. Using a spatial light modulator combined with the measurement of TM has been successfully used in the scanning configuration in fluorescence imaging [61, 62, 96] and micro-manipulation [61, 96].

Imaging plane and variation of its distances from the fibre facet
The TM measurement can be performed at various distances from the fibre facet creating the focal spot at a defined working distance from the output fibre facet. The field of view (FOV) at the output fibre facet is given by the size of the core. Increasing the working distance, the FOV increases, but the resolution determined by the numerical aperture (NA) decreases.
The intensity in the graph of Fig. 2.7 reflects the variation in the NA with the distance from the fibre facet. The maximal NA can be reached only in a cone with a base corresponding to the fibre core and the distance *H* given as

$$H = \frac{d_{core}}{2\mathrm{NA}}, \tag{2.24}$$

where d_{core} is the diameter of the fiber core [61]. For the fibre used in our experiments (diameter of 50 μm, NA 0.22) the distance $H \approx 114$ μm. We typically set the working distance to ~30 μm which ensured diffraction-limited resolution across most of the FOV.

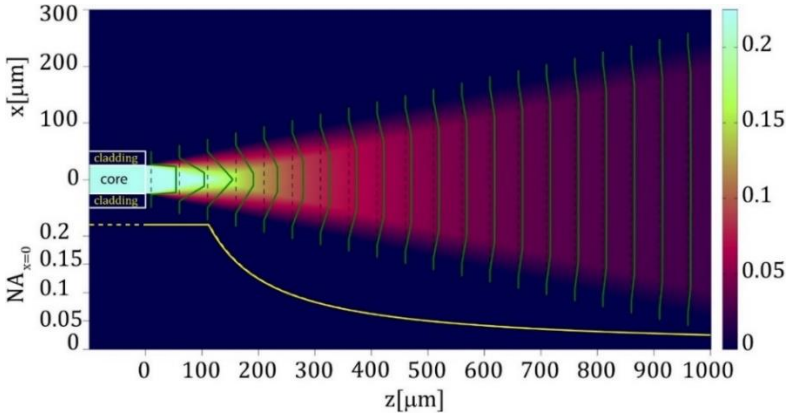

Figure 2.7: Evolution of the numerical aperture at different distances from the fibre facet [61]. The green lines indicate the NA profile in transversal planes and the yellow line show the maximum NA along the optical axis *z*. Imaging further from the facet, the distance in which the resolution is still limited by diffraction depends on the NA in the given location.

2.6 Imaging through the MMF with calibrated foci

The holograms calculated for all output modes are projected sequentially, yielding a scanning focal spot in the focal plane. The maximum scanning speed is determined by the refresh rate of the DMD (22 kHz). For fibre used in our experiments, this corresponds to 3.5 fps for the full field of view – 50 μm in diameter (see Fig. 2.8). In fluorescent imaging, the scanned focal spot excites the fluorescence signal from the sample, which is collected and propagates backwords through the same MMF at the output spectrally filtrated (F, Fig. 2.4) and detected on a sensitive detector – photomultiplier tube (PMT)Its acquisition frequency is synchronized with the scanning rate of the DMD.

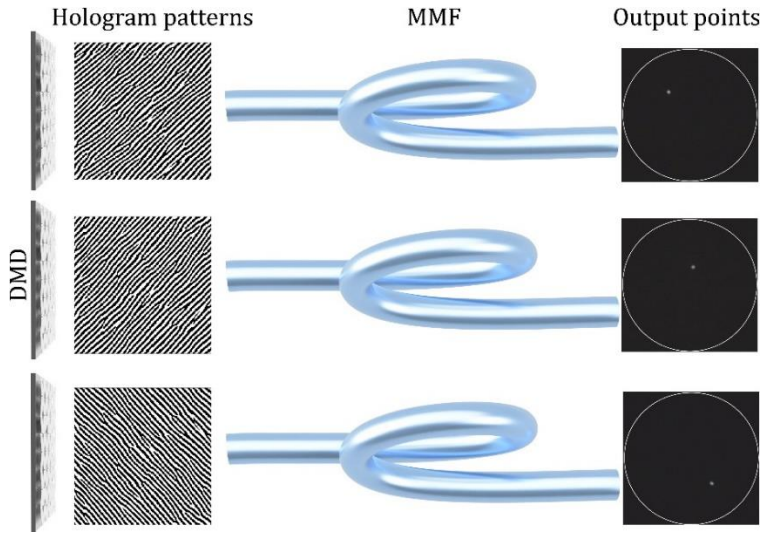

Figure 2.8: Patterns projected on the DMD and the corresponding output focal spots.

3. Results

In this chapter I first present the conditions that need to be met for high quality imaging using the holographic endoscope (Section 3.1) and demonstrate imaging of a two-dimensional and three-dimensional fluorescent phantom sample (Sections 3.2 and 3.3). Next, I present a method that allows to enhance the image quality via post-processing (Section 3.4). In Section 3.5 I summarize procedures that we used for the acquisition of brain samples from live mice expressing a suitable fluorescent protein. In Section 3.6. I demonstrate the principle and verification of the effect of confocal endo-microscopy.

3.1 Quality of the scanning spot

The quality of the fluorescence image in holographic micro-endoscopy is strongly affected by the quality of the scanning spot. After calibration using phase-only modulation, the scanning spot carries only a fraction of the optical power compared to the full power delivered by the MMF (Fig. 3.1a). It has the shape of a high-intensity peak surrounded by a series of concentric rings (Fig. 3.1b bottom). The remaining fraction of light is dispersed as a random background pattern (Fig. 3.1a, bottom). This is typically quantified by the "power ratio" (PR) given by the ratio between the power in the spot and the total output power [71]. PR = 1 describes an ideal focal spot without any background while PR = 0 is essentially random speckles.

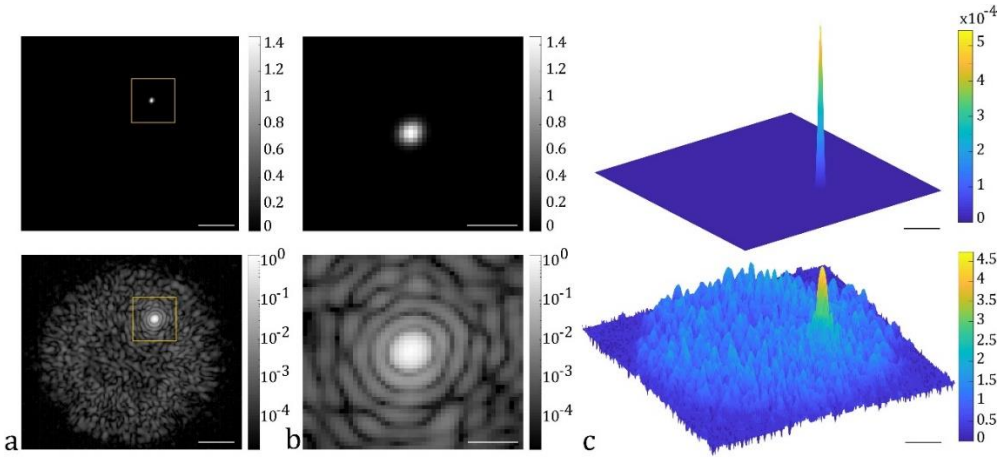

Figure 3.1: Calibrated focal spot. a) Example intensity image of a focal spot generated through the MMF with PR = 75 %. The speckled background is visible from the log-scale image (bottom). Scale bar is 10 μm. b) Zoomed-in images of the focal spot. Scale bar is 2.5 μm. c) 3D visualisation of the focal spot. Scale bar is 10 μm.

One of the reasons for PR drop is that the MMF can randomize the polarisation of the propagated light implying that both polarizations should be modulated separately. Short segments of MMFs have been shown however to maintain circular polarization quite well [70, 71]. Another significant drop of PR is caused by modulation of phase rather than the complex modulation of light. DMDs could be theoretically used in the regime of complex modulation but at a cost of significant power losses [93] which for imaging *in vivo* with the laser available to us was not desirable. Therefore, we used the phase-only modulation of light in the off-axis regime as detailed in [87] and the maximum PR reached 79% [69].

For high imaging quality we strive to achieve high stable PR for hours. The stability of PR is affected by the stability of the setup and the environment, the changes in the temperature. The unstable temperature cause mainly changes of light polarization within single-mode fibres (SMF). A polarizer plate located at the output of the SMF filters and stabilises the polarization before the light beam reaches the DMD. Another component highly dependent on temperature is the DMD chip. During the calibration and imaging, the DMD chip is heating by high-frequency switching of the mirrors. This heating causes the deformation of micro-mirrors leading to wavefront deviations changing the input points phases of the modulated wavefront, which are different from the originally measured phase-shifts [97]. Thus, the PR

visibly degrades during time causing decrease of the contrast and resolution of the scanned images. To stabilize the PR, we mounted a thermoelectric cooler (TEC) with a Peltier and a heat sink at the back of the DMD module. The temperature of the TEC was set to temperature between the scanning and the resting regime of the DMD: 32℃. The TEC cools the DMD while scanning and heats it when at rest, stabilizing the temperature in the range of ±0.2℃ [97]. After these modifications, satisfactory long-term stability of the PR has been achieved. During the 50-hours measurement, the PR dropped only by 5% (Fig. 3.2), which is satisfactory for *in vivo* imaging.

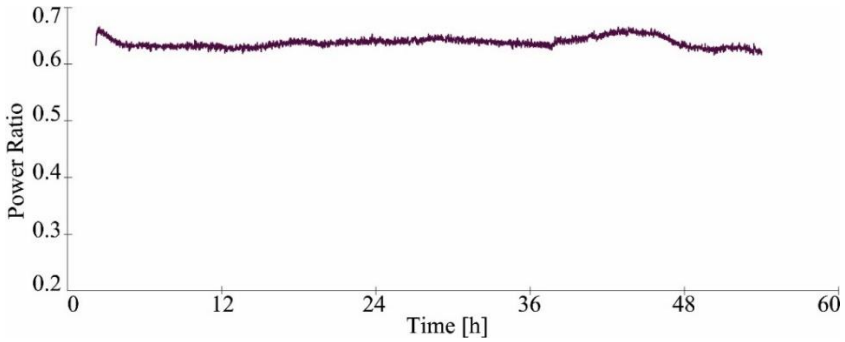

Figure 3.2: Performance of the stabilised setup. The PR dropped only by ~5% in 50 hours.

3.2 Fluorescence imaging of a two-dimensional phantom sample

We tested the imaging performance with fluorescent microspheres with a diameter of 2 μm (FluoSpheres™ Carboxylate-Modified Microspheres, 2.0 μm, Nile Red fluorescent (535/575), 2% solids, ThermoFisher Scientific) dispersed in distilled water in a ratio of 1:1000. The microspheres suspension was applied on a 0.17 mm thick cover glass and left to dry. The optical fibre was calibrated at a working distance of ~25-35 μm. The focal spots were scanned across the whole field of view (dia ~50 μm) with a speed of 3.5 fps (Fig. 3.3).

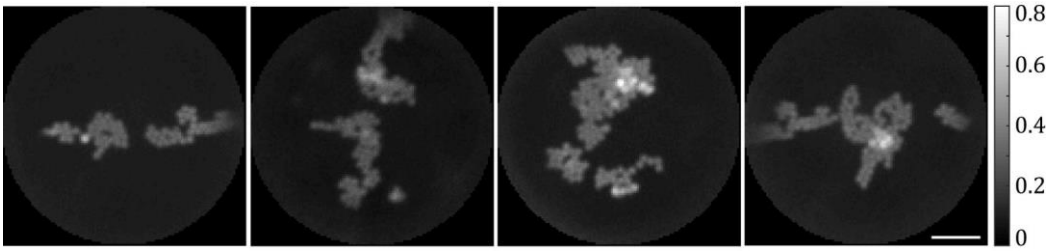

Figure 3.3: Example FOV of fluorescent microspheres on a cover glass. Scale bar is 10 μm.

3.3 Fluorescence imaging of a volume phantom sample

the MMF-based endoscope, the refocusing within a sample can be done by moving the probe inside the tissue. However, for short-distance refocusing the moving probe deforms the tissue [100].

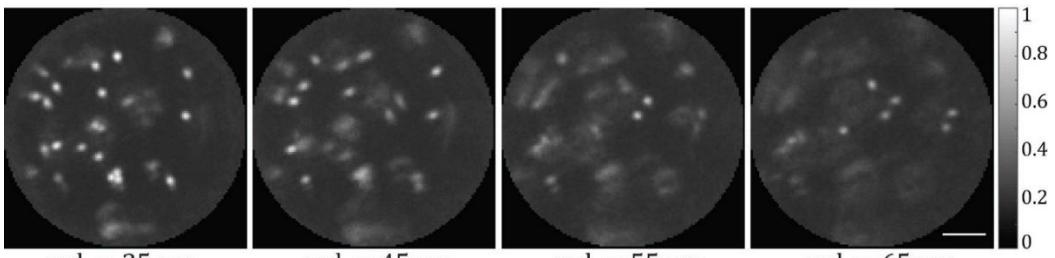

Figure 3.4: Imaging of a 3D phantom sample of fluorescent microspheres dispersed in an agarose gel. The sample was refocused by 10 μm in 3 steps. Calibration was performed at working distances (wd) 35, 45, 55 and 65 μm from the fibre facet. Scale bar is 10 μm.

The calibration for 4 different working distances (Fig. 3.4) was done sequentially for each plane by measuring the corresponding TM. A 3D fluorescent sample was prepared by dispersion of fluorescent microspheres (Nile Red, 2.0 μm in dia) in 0.5% agarose gel applying a 3 mm-thick layer to a cover glass. For imaging the MMF was inserted into the sample and refocusing to different depths was done by loading the appropriate set of holograms (Fig. 3.4). Refocusing without physical movement of the probe can be used with advantage in imaging *in vivo*, where the minimization of tissue displacement and damage is of high importance.

3.4 Computational Image Enhancement - harnessing the *muddy modes*

As discussed in Section 3.1, the maximum PR for phase-only modulation is 79%. The speckled background falsely contributes to the signal and decreases the dynamic range of the images. This effect is very significant in brain tissue where thin neuronal processes surround very bright cell bodies.
Knowing the shape of the PSF, the images can be reconstructed with higher resolution and contrast using deconvolution. In the case of endoscopic imaging, the PSF has a shape of the focal spot with speckled background unique for every position of the focus. We call these structures the *muddy modes*, which are reproducible. Therefore, we proposed a similar approach to the deconvolution using records of all muddy modes used for imaging.

A single intensity measurement r_i in the *i*-th pixel recorded by the PMT can be expressed as the sum of the illumination intensity across all pixels (one muddy mode) weighted by the density of fluorophores in the sample **s**. The illumination patterns, the focal spot and background measured with the camera, are stored in a muddy-mode matrix **M**, where each row contains one muddy mode flattened into a vector. The sample **s** is arranged into a column vector hence **r** can be written in the form of a forward problem as a linear transformation

$$\mathbf{r} = \mathbf{M}\mathbf{s}. \tag{3.1}$$

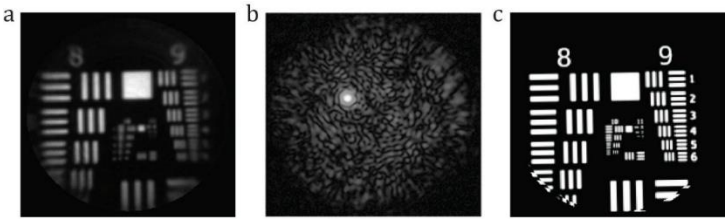

Figure 3.5: The detected image r (a), captured image of the n^{th} muddy mode M_n (b) and the sample **s** - fluorescent USAF target.

If we measure both **r** and **M** in Eq. (3.1), we can calculate the sample **s**. One could find the solution for **s** using a direct matrix inversion. However, due to the presence of noise in both **r** and **M**, the resulting image would be of poor quality. Therefore, we proposed two approaches for retrieving the sample considering the noise. One approach is based on a regularised iterative inversion algorithm, respecting the Poisson noise distribution (PN) in the measured signal. The second exploits a simple regularised direct pseudo-inversion algorithm originally designed for an intensity invariant noise (INN). The algorithms can be used to optimize the contrast and resolution of the image.

Reconstruction algorithm for images with a Poisson noise (PN)

When imaging through the MMF a Poisson noise distribution in the recorded signal **r** can be expected due to the nature of a photon-detection process [98]. We confirmed this by measuring the variance of the recorded signal (Fig. 3.6). The distribution of the real sample **s** (the most probable values of **s** solving Eq. (3.1)) can be found using the maximum likelihood estimation. To find the inverse solution of Eq. (3.1), one can use an iterative scheme [see Eq. (21) in 98] (assuming zero background) with one of the simplest regularisation functions is known as an L_2-norm giving a preference to solutions with smaller norms

$$\mathbf{s}^{(i+1)} = \frac{\mathbf{s}^{(i)}}{\mathbf{1} + \frac{\mathbf{1}}{\mathbf{2}}\boldsymbol{\lambda}\boldsymbol{\nabla}\left\|\mathbf{s}^{(i)}\right\|^2}\left[\mathbf{M}^{\boldsymbol{T}}\frac{\boldsymbol{r}}{\mathbf{M}\mathbf{s}^{(i)}}\right], \tag{3.2}$$

where $s^{(i)}$ and $s^{(i+1)}$ are the sought solutions in the i^{th} and $(i+1)^{\text{th}}$ iteration steps, respectively. $\lambda \geq 0$ is a regularisation factor determining the strength of the applied regularisation and ∇ is the operator of function gradient. The solution of inverse problems with this type of regularisation is often referred to as the Tikhonov, or ridge regularisation [99].

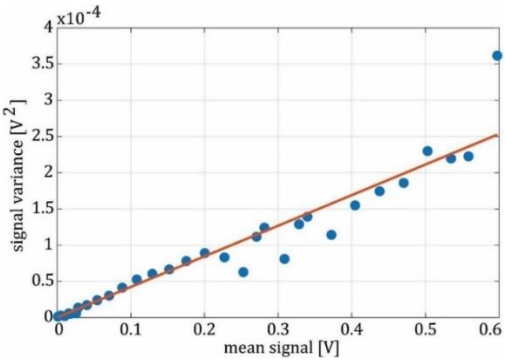

Figure 3.6: Variance of the recorded voltage from the PMT as a function of its mean (blue dots) and the linear interpolation (red).

Reconstruction algorithm for images with an intensity independent noise (IIN)

In the second approach we use the algorithm which presumes an intensity independent noise distribution in the recorded signal **r**. This assumption is not correct in general for an imaging process; however, it allows to search for the solution of Eq. (3.1) by minimization of a least-squares problem

$$\Psi = \sum_{i=1\ldots n_{\mathrm{r}}} [(\mathbf{M}\mathbf{s})_i - r_i]^2 + \lambda\mathcal{R}(\mathbf{s}) \tag{3.3}$$

where $\lambda\mathcal{R}(\mathbf{s})$ represents the regularisation term and λ is a regularisation factor. In an absence of any regularisation, Eq. (3.3) could be solved using pseudo-invers of **M**. This can be computed with a singular value decomposition (SVD) and **M** can be thus written as:

$$\mathbf{M} = \mathbf{U}\Sigma\mathbf{V}^T, \tag{3.4}$$

where **U** and **V** are orthogonal matrices and Σ is a rectangular matrix of singular values σ_i in diagonal. The pseudo-inverse matrix $\mathbf{M}^+$ can be expressed as $\mathbf{M}^+ = \mathbf{V}\Sigma^+\mathbf{U}^T$. The matrix Σ^+ is the pseudo-inverse of Σ, where each diagonal element is replaced by its reciprocal value. With the regularisation term present in Eq. (3.3), its minimum can also be found using the SVD. The solution can be found by adjusting the diagonal values of Σ^+, where all non-diagonal values remain zero. The regularised pseudo-inverse can then be expressed as

$$\mathbf{M}^{+'} = \mathbf{V}\Sigma^{+'}\mathbf{U}^T \tag{3.5}$$

and an efficient estimate of the sample can be obtained from

$$\mathbf{s} = \mathbf{M}^{+'}\mathbf{r}. \tag{3.6}$$

The pseudo-inversion for a single regularisation strength λ has to be performed only once and the solution of the inverse problem constitutes a simple and fast matrix-vector multiplication. Some negative values may still occur in the image as a result of e.g. the detector dark noise (Fig. 3.7). A solution with a small fraction of negative values may be acceptable.

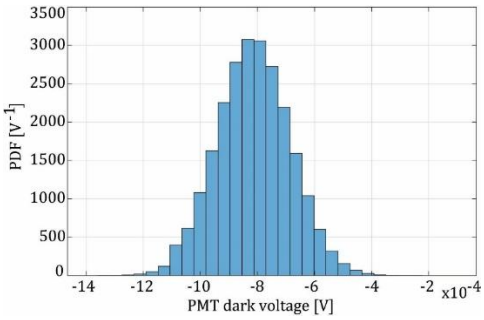

Figure 3.7: The probability density function (PDF) of PMT dark noise.

Experimental setup and sample preparation

For the experimental measurement, we have used our optical setup (Fig. 2.5) whose simplified geometry is presented in Fig. 3.8 outlining all steps of the procedure. The calibration part was done as described previously (Section 2.5). The holograms are displayed on the DMD, and the muddy modes are raster-scanned across the imaging plane at the focal plane.

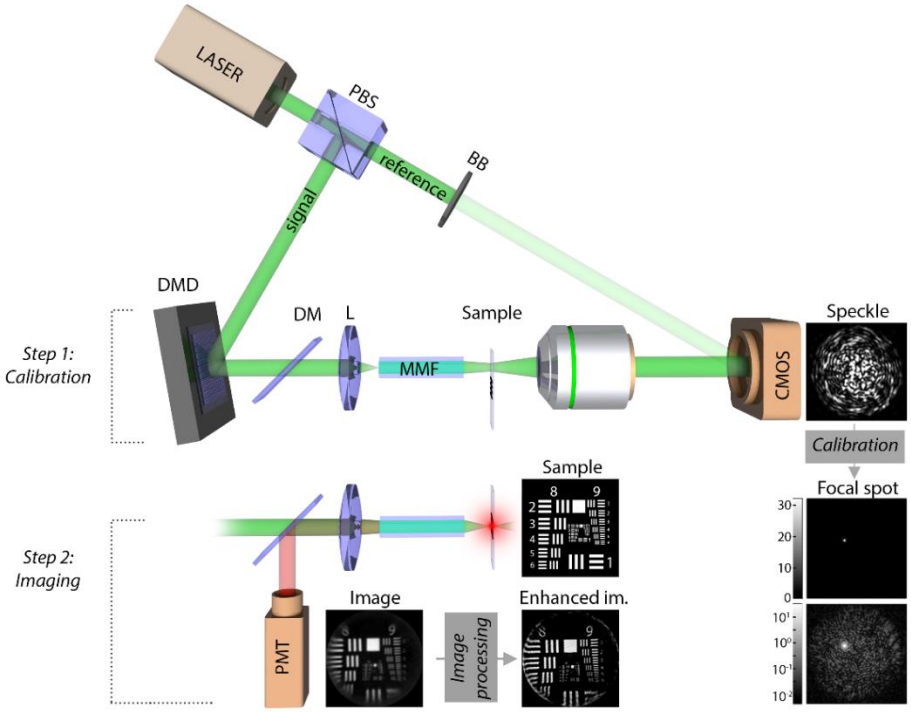

Figure 3.8: Simplified endoscope setup and the flow of calibration, imaging, and image enhancement procedures. After calibration, the intensity of the focal spot with background signal - muddy mode, is measured. A fluorescent signal from the sample (USAF target) is detected on a PMT and the resulting image is post-processed by the reconstruction algorithms. The result is an enhanced image with higher contrast and resolution.

The intensity distribution of every muddy mode is recorded on the camera and saved for the computational image enhancement. Due to the insufficient dynamic range of the CMOS camera, we implemented an image capturing technique of a high-dynamic range (HDR). Every muddy mode was recorded with three different camera exposure times - 10, 100 and 1000 μs. For the experiment, we measured 34 894 muddy modes with foci organized across a rectangular grid with a period of 225 nm. For the image acquisition the fluorescent sample was inserted under the MMF into its focal plane and scanned across the whole FOV corresponding to ~50 μm with a refresh rate of the DMD of ~0.5 full scans fps.

Our sample was a fluorescent USAF target (Fig. 3.9a) which allowed us to measure contrast of distinct spatial frequencies directly related to image resolution. The sample (Fig. 3.9b) was prepared from a fluorescent layer of Rhodamine B with spacers of 5 μm in diameter in between a cover glass and an in-house made USAF target deposited on a cover glass.

The dependence of image contrast on spatial frequencies can be described by a contrast transfer function (CTF). We measured the contrast from regions indicated in Fig. 3.10a. The selected elements 2-4 from group 8 and elements 1-6 from group 9 have theoretical spatial frequencies $f_{8,2} = 287.4\,mm^{-1}$, $f_{8,3} = 322.5\,mm^{-1}$, $f_{8,4} = 362.0\ \ mm^{-1}$ and $f_{9,1} = 512.0\,mm^{-1}$, $f_{9,2} = 574.7\,mm^{-1}$, $f_{9,3} = 645.1\,mm^{-1}$, $f_{9,4} = 724.1\,mm^{-1}$, $f_{9,5} = 812.7\,mm^{-1}$and $f_{9,6} = 912.3\,mm^{-1}$, respectively. Figure 3.10b shows the CTF measured from the image (red points) and a theoretical CTF corresponding to an aberration-free imaging system with a circular aperture and numerical aperture NA = 0.22, i.e. NA of the MMF fibre used for imaging (blue).

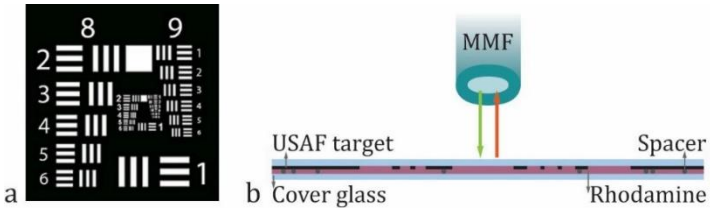

Figure 3.9: A fluorescent USAF target sample. a) An USAF target with groups 8 and 9 selected for deposition to serve as the fluorescent sample. b) The structure of the fluorescent USAF target deposited on a cover glass with a layer of Rhodamine and spherical spacers enclosed by a second cover glass.

Criteria for evaluation of image quality

To determine the quality of the reconstructed image, we compare it to a "ground truth" image of the USAF target (Fig. 3.10c) obtained by scanning electron microscopy, binarized, scaled down to the desired pixel resolution and registered to the reconstructed image.

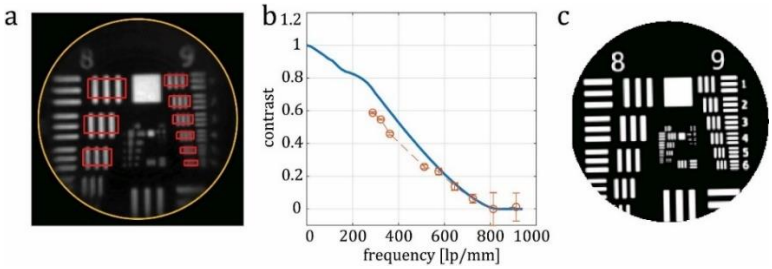

Figure 3.10: USAF target imaged by point scanning. a) Experimentally obtained image of the USAF target with regions of interest used for computation of the contrast (red) and with an area corresponding to the FOV of the MMF (yellow). b) CTF calculated from the indicated regions in (a) (red) and a theoretical CTF (blue), error bars represent the 95% confidence intervals. c) "ground truth" image.

One of the common measures is the peak signal-to-noise ratio (PSNR) [101] defined as

$$\mathrm{PSNR} = 10\log_{10}\left[\frac{1}{\mathrm{MSE}}\right], \mathrm{MSE} = \frac{1}{n_s}\sum_{i=1\ldots n_s}[\beta \mathbf{s}_i - \mathbf{t}_i]^2 \qquad (3.7)$$

MSE represents the mean squared error, n_s is number of pixels forming the reconstructed sample $\mathbf{s}$, $\boldsymbol{s_i}$ and $\boldsymbol{t_i}$ represent the intensity of i-th pixel of the recorded or reconstructed image and "ground truth", respectively. A scaling factor β allows us to maximize the PSNR for each regularised strength and compare the corresponding PSNR values due to change of the dynamic range of the reconstructed image.

Another approach considering the human perception is the Structural Similarity Index (SSIM) [100]. The method assesses the visual impact of luminance, contrast and structure of the image and can be described as

$$\mathrm{SSIM} = \frac{(2\mu_s\mu_t + c_1)(2\sigma_{st} + c_2)}{(\mu_s^2 + \mu_t^2 + c_1)(\sigma_s^2\sigma_t^2 + c_2)}, \tag{3.8}$$

where μ_s and μ_t are the means, σ_s and σ_t are the standard deviations, σ_{st} is the cross-covariance for images **s** and **t**, respectively, and c_1 and c_2 are small constants used to prevent zero division. The SSIM demonstrates how the human eye perceives a difference between 2 images in a range of 0 (images with no similarity) to 1 (identical images).

Image enhancement with Poisson noise (PN)

The enhanced images from experimentally obtained data are calculated for various values of the regularisation factor λ using Eq. (3.2). The initial guess of solution $s^{(0)}$ is selected as uniform over the field with intensity corresponding to mean value of the original image. Figure 3.11a presents the set of reconstructed images, the original image. The corresponding CTFs are plotted in Fig. 3.11b.

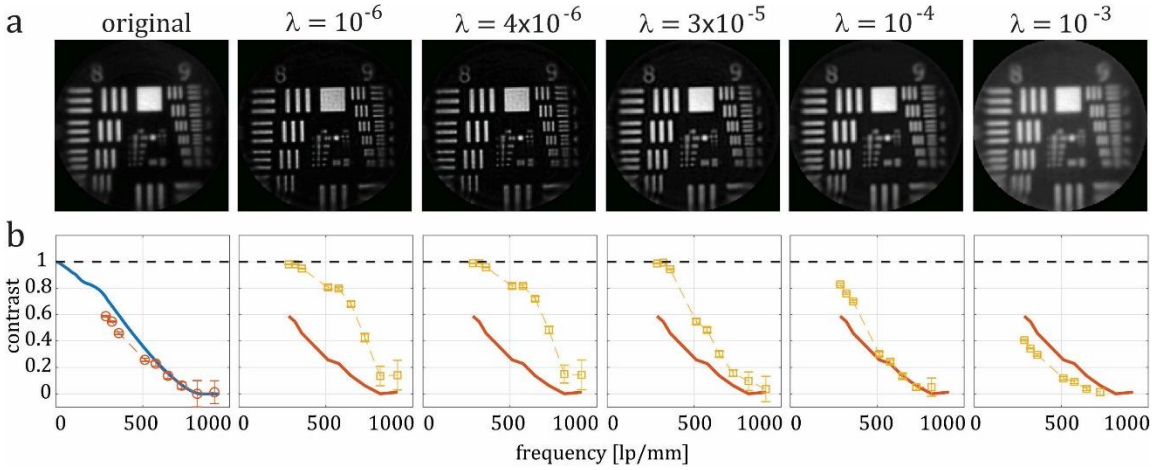

Figure 3.11: The effect of λ on reconstructed images using the PN-based inversion. a) Image of the USAF target obtained by scanning the fluorescent sample via the MMF (original) and image reconstructions for different values of λ. b) Corresponding CTFs: theoretical (blue), CTF calculated from the original image (red) and from the reconstructed images (yellow), respectively. Error bars represent the 95% confidence intervals.

A maximum contrast 1 is delineated by dashed black line in graphs. The blue curve represents the theoretical CTF, the red curve has been calculated from the acquired image and compared to the CTFs calculated from the reconstructed images (yellow). The contrast of all analysed spatial frequencies can be enhanced, and it can be determined, which value of λ is the most effective.

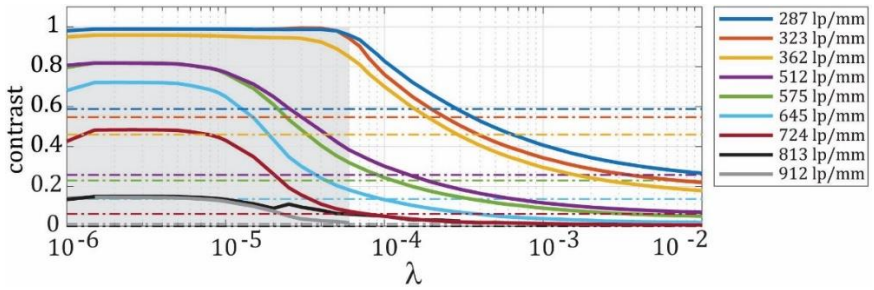

Figure 3.12: Mean contrast across resolved USAF target elements as a function of λ. Each colour represents a different spatial frequency, the dash-dotted horizontal lines show the contrast of the corresponding spatial frequency in the original image. The grey area indicates the region in which the contrast has been enhanced for all evaluated spatial frequencies.

The evolution of contrast of different spatial frequencies with λ is presented in Fig. 3.12. For frequencies ≤ 323 lp/mm (line pairs per millimetre), the contrast can be enhanced up to ~ 0.99 for $\lambda < 5 \times 10^{-5}$. The grey area highlights a common range of $\lambda < 6 \times 10^{-5}$ for which the contrast has been enhanced for all spatial frequencies. The contrast curves plateau for λ in the range of $1.5 \times 10^{-6} \leq \lambda \leq 5 \times 10^{-6}$ corresponding to enhancement by 68% (for the lowest frequency) and more.
Figure 3.13 depicts PSNR (blue) and SSIM (red) as a function of λ. The corresponding values from original image are represented by dashed lines (11.36 dB and 0.31, respectively).

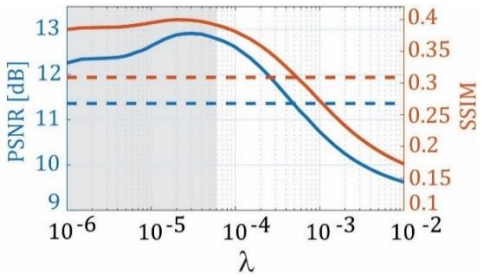

Figure 3.13: PSNR and SSIM of the reconstructed images as a function of λ. Dashed lines represent the PSNR and SSIM of the original image, 11.36 dB and 0.31, respectively. The grey region highlights the range of λ with enhanced contrast for all spatial frequencies.

According to PSNR metric, the reconstructed images are enhanced for $\lambda < 5 \times 10^{-4}$ reaching maximum of 12.91 dB (an enhancement of $\sim 14\%$). According to the SSIM metric the images are enhanced in the same λ interval of with maximum reaching 0.4 (an enhancement of 29%). Both metrics reach their maximal values close to $\lambda \sim 3 \times 10^{-5}$.

These results imply that the optimal choice of the regularisation factor is a value in the range $5 \times 10^{-6} \leq \lambda \leq 3 \times 10^{-5}$, leading to enhancement of all three metrics.

Image enhancement with the IIN

The image reconstructions for the case of intensity-independent-noise (IIN) - based inverse modelling were calculated using Eqs. 3.5 and 3.6. Figure 3.14a shows the original image and sample reconstructions for different values of λ.
The values of $\lambda < 0.22$ give reconstructions with negative values which fraction strongly increases with decreasing of λ. The threshold for negative pixels was set to 1% of the total pixel count, which is fulfilled for $\lambda \geq 0.16$. For the high values of λ the transformation operates as a low-pass filter slightly decreasing the contrast of low frequencies and suppressing the contrast of high ones. As a result, we receive a smoothed image with the resolution lower than the original, which can be seen in Fig. 3.14 for $\lambda = 5$. The CTFs corresponding to the images in panel (a) are plotted in Fig. 3.14b. Negative values in reconstructions with $\lambda < 0.16$ were replaced by zeros, therefore the calculated contrast is not artificially increased. The quality of enhancement is evaluated by the average contrast enhancement for each resolved spatial frequency as a function of λ shown in graph in Fig. 3.15. Again, the reference values calculated from the original image are plotted as dash-dotted lines in the same colour code. For frequencies ≤ 323 lp/mm the contrast can be enhanced up to 1 using regularisation factor $\lambda = 0.16$.

Enhanced contrast for all spatial frequencies is highlighted as the grey area in a range of $0.16 \leq \lambda \leq 0.18$, which is very narrow. Selecting higher λ (up to 0.47) will result in an increase of contrast of the lower spatial frequencies but decrease of the higher ones. The contrast curves peak for $\lambda \leq 0.016$, which is among the unacceptable solutions plotted in dotted curves. The maximum acceptable contrast enhancement is therefore for $\lambda = 0.16$, which corresponds to enhancement by 69% (for the lowest frequency) and more (for higher frequencies).

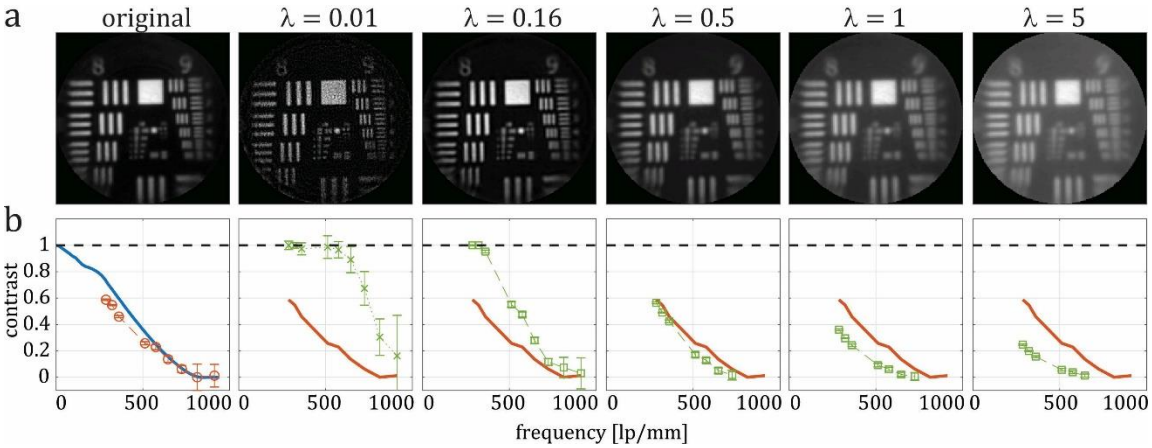

Figure 3.14: The effect of λ on reconstructed images using the inversion with IIN. a) Image of the USAF target obtained by scanning the fluorescent sample via the MMF (original) and image reconstructions for different values of λ. b) Corresponding CTFs: theoretical (blue), CTF calculated from the original image (red) and from the reconstructed images (green), respectively. A dashed line represents the maximum contrast of 1. Error bars represent the 95% confidence intervals.

The graph in Fig. 3.16 shows the PSNR (blue curve) and SSIM (red curve) comparison of the enhanced images and their values from original images (dashed lines). The original values are 11.36 dB for PSNR and 0.31 for SSIM.

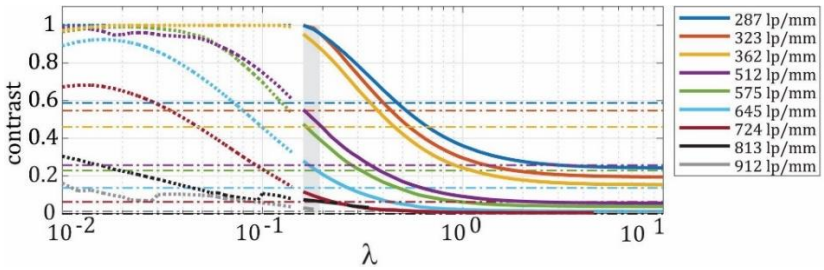

Figure 3.15: Mean contrast across the resolved USAF target elements as a function of λ. The grey area indicates the interval of acceptable solutions for which the contrast of all evaluated spatial frequencies has been enhanced. The dotted segments indicate unacceptable solutions.

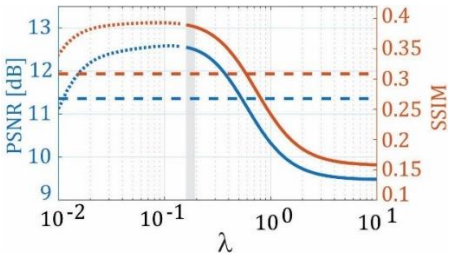

Figure 3.16: PSNR and SSIM of the reconstructed images as a function of λ. The dotted part of the curves indicates unacceptable solutions. The grey region indicates the interval of λ with enhanced contrast for all spatial frequencies as in Figure 3.15.

The PSNR metric is enhanced in a range of $0.16 \leq \lambda \leq 0.55$, where the maximum of 12.55 dB is for $\lambda = 0.16$ (an enhancement by 10 %). The SSIM metric is enhanced over a range of $0.16 \leq \lambda_R \leq 0.6$ with maximal value of 0.39 for $\lambda = 0.16$ as well (an enhancement of ~26 %).

In order to test and confirm the concept in conditions similar to the biologically relevant imaging we have imaged fluorescent microspheres. The sample was prepared by dispersing the fluorescent microspheres (Nile Red, 2.0 μm in dia) in a distilled water (1:1000) and let dry on a cover glass. Both algorithms succeed to enhance the contrast, reduce the background and increase the resolution, even

with sub-optimal conditions. Figure 3.17b compares the intensity profiles along fluorescent microspheres in the original image (red lines 1 and 2) and the reconstructed images using the PN-based algorithm with selected value of $\lambda = 5 \times 10^{-6}$ and the IIN-based reconstruction with $\lambda = 0.16$. Both methods yield an increased contrast, the PN-based algorithm slightly outperforming the IIN-based one.

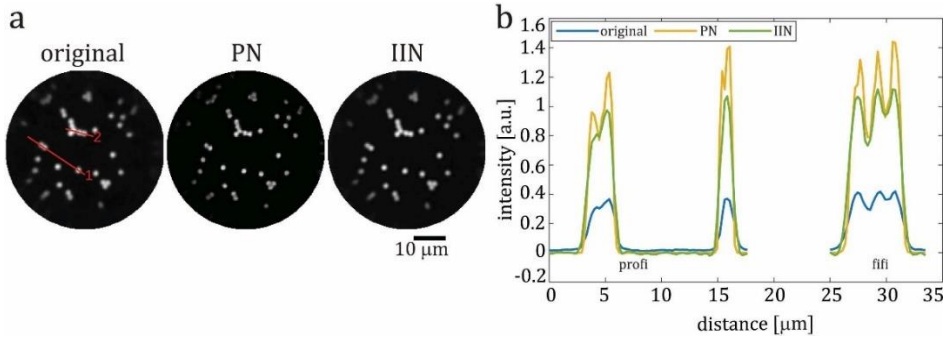

Figure 3.17: Image enhancement of fluorescent micro-particles. a) normalized images of scanned fluorescent microspheres (original) and its reconstruction based on the PN and IIN method. b) Comparison of intensities in profile 1 and 2 (red, original image).

The same optimal value of regularisation factor λ derived from a single image can be used for image enhancement of a series of images of a changing FOV from the sample (PN and IIN in Fig. 3.18).

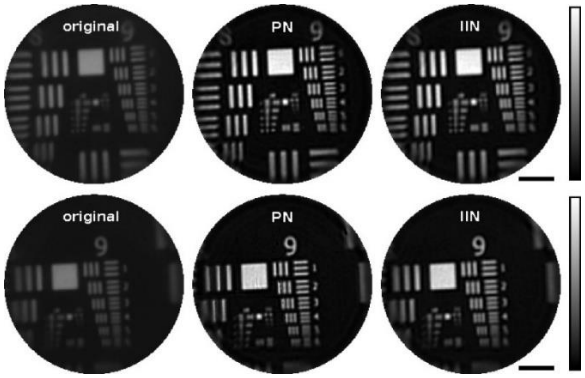

Figure 3.18: Example of 2 field of views from fluorescent imaging of USAF target. For the image enhancement the same optimal values of λ were selected as in Fig. 3.17. Scale bar is 10 µm.

3.5 Imaging of mouse brain tissue

In order to advance the application of MMF-based endoscope to *in vitro* and *in vivo* imaging, it was important to identify a suitable mouse model and master the technique for preparation of the animal brain for the experiment.

3.5.1 Mouse model with sparse fluorescence expression

When imaging through MMF, the 3D sample is illuminated with a PSF. It causes speckled background and a conical shape along the *z*-axis, excitating the fluorescent signal from the selected object and from the surrounding tissue. The sample with high density of fluorescent sources thus gives images with poor contrast and sub-optimal resolution. These issues can be partially alleviated by modulation of the sparsity of fluorescent objects and decreasing their density. One way to modulate such sparsity can be genetic engineering, used in our experiments. By cross-breeding of the genetically modified mouse lines only the required cell types can express the fluorescein protein and also their amount can be controlled.

Selection of mouse models for cross-breeding

For the *in vitro* and potentially *in vivo* imaging of neuronal networks we identified a genetically modified mouse model with a red fluorescent protein tdTomato conditionally expressed in excitatory

neurons, mostly present in cerebral cortex and also in hippocampus [102, 103, 104]. This mouse line was obtained by breeding a transgenic line B6.Cg-*Gt(ROSA)26Sor*$^{tm14(CAG-tdTomato)Hze}$/J (007914, Jackson Laboratory, USA) crossed with a Cre-recombinase- expressing mouse line B6;129S6-Tg(Camk2a-cre/ERT2)1Aibs/J (012362, Jackson Laboratory, USA).

Figure 3.19 shows schematically the breeding process. One mouse line has a fluorescent protein tdTomato coded behind a promotor of the gene (R26) ubiquitously expressed in every cell in the mouse body and a STOP sequence in between. The second mouse line has a Cre-recombinase coded behind the promotor specifics for a selected population of cells (Camk2a for excitatory neurons) and after cross-breeding it cuts out the STOP sequence in cells defined by the specific promoter leading to expression of the fluorescence protein. However, the selected Cre line has a Hitshot protein 90 (HSP90) bound to an estrogen receptor ERT (Fig. 3.19c) inhibiting the Cre-recombinase. After injection of Tamoxifen, it cuts out the HSP90 in the cytoplasm and bounds to the ERT. The Cre-recombinase is activated, penetrates the nucleus of the cell, and cuts out the STOP sequence (Fig. 3.19d). Using Tamoxifen, it is thus possible to regulate the density of the fluorescence protein expression.

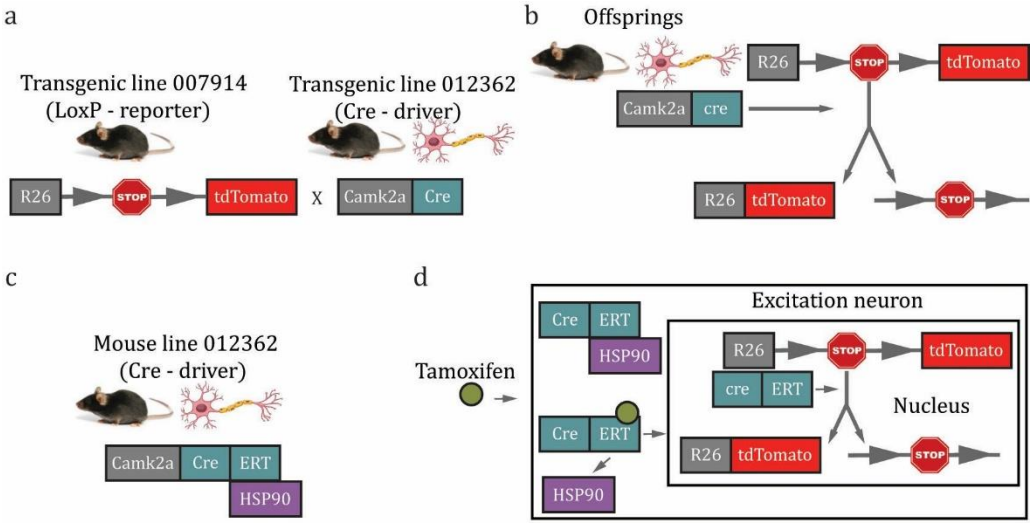

Figure 3.19: Scheme for breading of the genetically modified mouse carrying the fluorescent protein expressed in excitatory cells. a) Mouse line carrying the fluorescent protein cross bread with a mouse line carrying the Cre-recombinase. b) The Cre-recombinase cuts out the STOP enabling the tdTomato to be expressed in excitatory neurons. c) The Hitshot protein 90 inhibiting the Cre-recombinase. d) Effect of Tamoxifen on activation of the Cre-recombinase leading to the expression of the R26tdTomato sequence.

Genotypization

When the offsprings are born, it is necessary to confirm the presence of the desired fluorescent protein. This was done by genotypization only of the heterozygous gene (driver mice, reporter mice are homozygous). For the DNA extraction we used the REDExtract-N-Amp^{TM} Tissue PCR Kit (Sigma-Aldrich). A tissue sample (2-10 mg) is immersed for 10 minutes in the mix of the 25 µl Extraction and 6.25 µl of Tissue solutions. The mixture is 1 min vortexed, incubated at 90° for 3 minutes and 1 min vortexed. The 25 µl of Neutralization solution is added, the whole solution is vortexed and stored at 4°C. For a polymerase chain reaction - PCR was prepared solution with a total volume of 5 µl. To the 2.5 µl of the REDExtract-N-Amp PCR Reaction Mix solution we add 1.5 µl of a mix of two primers (forward and reverse) and we add 1 µl of the neutralized DNA extract from mouse tissue sample. We also use a control sample known to containing required gene. The mixed solutions are placed into the PCR Thermal Cycler (BioTech) and the amplification of DNA sequences than proceeds following the protocol from Table 3.1 in Appendix A.

The results of amplification are visualized using Electrophoresis of nucleic acids. For one electrophoresis we use 350 ml of the 1xTBE buffer (10x TBE Rotiphorese diluted in distilled water).

We prepare 1 gel of 0.56 g of the agarose powder (Sigma-Aldrich), 28 ml of 1xTBE buffer and 2.8 μl of SYBER. Dissolved agarose is poured out into the prepared chamber with the ladder to create small pits and let dry. To visualize the results, we add 1 μl of a blue dye buffer ROTI Load into the PCR sample. We submerge the gel under the TBE buffer in the electrophoresis box, add the sample, set the constant current to 140A and let it run for ~30 min. The resulting bands in the gel are imaged using a UV lamp and a filter. The presence of the gene confirms an animal with positive expression of the tdTomato protein.

3.5.2 Preparation of fixed mouse brain slices

For *in vitro* imaging the tissue sample is obtained according to a following protocol. The mouse positive for the tdTomato protein is put into an anaesthesia using 5% isoflurane in 0.8-1 l/min oxygen and intraperitoneally injected ketamine (0.05 μl) and xylazine (0.015 μl). The heart of a deep unconsciousness mouse is exposed by uncovering the thorax. The mouse is perfused by injecting the 4% paraformaldehyde (PFA) into the left ventricle. The extracted brain is fixed in 4% PFA for ~30-72 hours at 4°C. Then the brain is washed and stored in Phosphate Buffered Saline – PBS at 4°C. Brain slices of 50-200 μm thick coronal sections are prepared on VT1200 vibratome (Leica), further stored in the PBS. All chemical solutions including brands are listed in Table 3.2 in Appendix A.

All animal procedures were conducted in accordance with protocols approved by the Branch Commission for Animal Welfare of the Ministry of Agriculture of the Czech Republic (permission No 47/2020). The surgical procedures and manipulation with the animal in the operating room and during experiment have been conducted by Tereza Tučková with a certificate number CZ 03422 of the licence approving her for experimental manipulation with laboratory animals.

3.5.3 Imaging of mouse brain slices

After calibration of the system (Section 2.5) with MMF immersed in the PBS, the brain slice fixed on a Petri dish is inserted under the MMF and the imaging is done with the probe outside the tissue. The results are shown in a set of images in Fig. 3.20. We can see the fluorescent signal from excitatory neurons. To distinguish finer structures (dendrites or axons) the contrast is too low, and the background fluorescence is high. In these samples we have reached the maximum sparsity of fluorescent cells. Despite that, the density of fluorescent neurons is rather abundant yielding low contrast of images, hardly distinguish the sub-cellular structures.

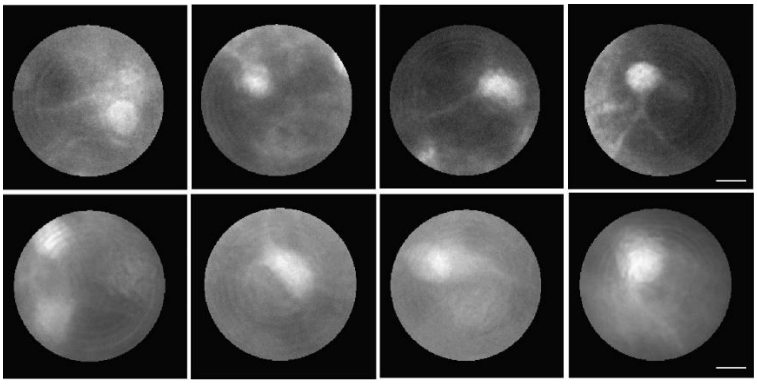

Figure 3.20: Examples from single-photon imaging through the MMF endoscope of excitatory neuronal networks expressing tdTomato in coronal section of the brain slices. The slices are thick 50 μm (top row) and 100 μm (bottom row). Scale bare is 10 μm.

As a reference, we acquired 2-photon excitation fluorescence microscopy images of the same sample and same region of interest (cortex) (Fig. 3.21). These observations have clearly identified the need for out-of-focus light attenuation. Therefore, we proposed a new concept of confocal endo-microscopy using a custom-designed fibre probe.

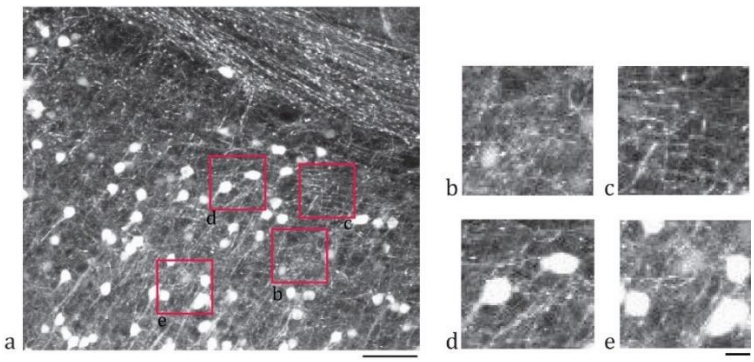

Figure 3.21: 2-photon microscopy images of brain slices of mouse-line expressing tdTomato in excitatory neurons. a) Maximum intensity projection of a z-stack containing 40 images 2 μm apart. The scale bar is 50 μm. b) – c) Zoomed-in regions of interest showing dendrites and spines. d) – e) Zoomed-in regions of interest of cells bodies. The scale bar for b) – e) is 10 μm and the size of FOVs is similar to the one acquired through the MMF.

3.6 Confocal imaging via MMF-based holographic endoscopy

In this chapter we present a new technique for out-of-focus light attenuation based on a new concept of MMF-based confocal holographic endoscopy, which can be practically utilized for imaging of fluorescent biological samples. Using fluorescent microspheres and fixed brain slices we demonstrate the principle and the proof of concept.

3.6.1 Multi-mode probe for confocal imaging

The vital component is a custom-developed probe consisting of a graded-index (GRIN) multi-mode fibre spliced with a step-index (SI) multi-mode fibre (GRIN-SI-MMF) (Fig. 3.22). A short segment of GRIN fibre length *1/4* of pitch length *P* images the object into infinity (similar to GRIN lens) and thus can be used for beam collimation. We use a commercially available GRIN fibre (GIF625, Thorlabs, diameter of 125 μm with core diameter of 62.5 μm and 0.275 NA) with $P = 1.056$ mm, shortened to $L = 220$ μm. At Fig. 3.22 a point source placed in the working distance d (30 μm for our case) is collimated by this GRIN segment transforming its Cartesian coordinates into an angular spectrum of plane waves at the proximal end of GRIN fibre, where they enter the SI fibre (FG050LGA, Thorlabs, diameter of 125 μm with core diameter of 50 mm and 0.22 NA) and propagate to its proximal side conserving the axial component of their *k* vectors [33, 61].

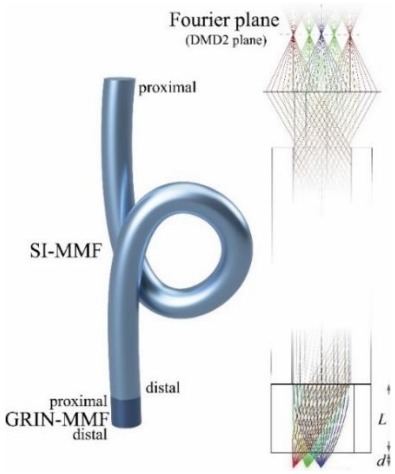

Figure 3.22: A confocal probe. a) The SI-MMF and the GRIN-MMF spliced together by their proximal and distal ends thus creating confocal probe. b) Illustration of the principle of light propagation through the SI-GRIN-MMF. The light from the point source at the imaging plane at distance *d* propagates through the GRIN-MMF of length *L* and enters the SI-MMF in the form of plane waves. Thus, plane waves come out from the proximal side of the fibre, and form an annular ring in the Fourier plane of the fibre.

Outcoming plane waves are imaged by a lens forming annular rings in the Fourier plane of the fibre. Changing the focal point position radially from the fibre axis (from red to the blue point in Fig. 3.22b) results only in the change of the ring diameter [33]. The light coming from outside of the focus in the focal plane will be imaged outside of the corresponding ring and can be filtered out using e.g. a DMD2 (Fig. 3.24). The light coming from outside of the focal plane will yield a defocused ring in the far-field and will be attenuated in the filtration process similarly as in a classical confocal microscope.

3.6.2 Experimental setup

The core of the endoscope setup and its calibration is similar to the one described previously (Sections 2.4 and 2.5). The combination of the lenses L5 and added L6 demagnify the pattern in the iris plane. The beam is reflected by a dichroic mirror (DM), collimated by the lens L7 and enters the proximal facet of the MMF in the form of a plane wave. This is required due to the phase-only modulation of the light for SI-GRIN-MMF probe imaging in the far field [105]. The outcoming light is combined with the reference beam and detected on the CMOS camera (Fig. 3.23 Cal.1). The TM is measured using the bases of input plane waves and output points. After calibration, the DMD hologram creates a ring-shaped field in the far field of the proximal end of the fibre, yielding a nice focal point with high PR at the output of the SI-GRIN-MMF probe.

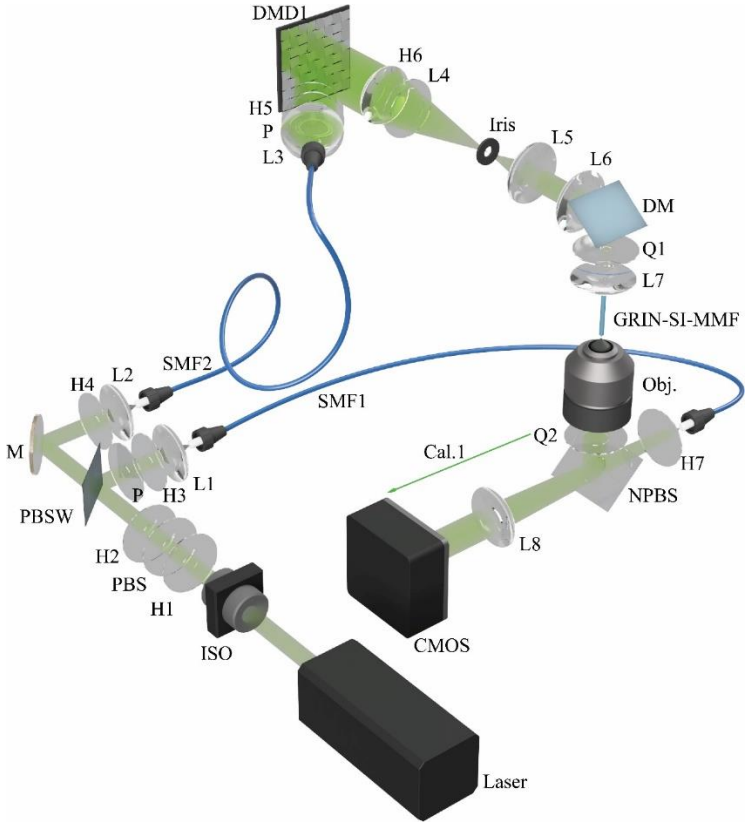

Figure 3.23: A part of the experimental setup intended for calibration of the scanning focal points. **M**: Mirror BB1-E01, Thorlabs, **PBS**: Polarizing Beam Splitter, CCM1-PBS25-532/M, Thorlabs, **H1-7**: Multi-Order Half-Wave Plate WPMH10M-532, Thorlabs, **PBSW**: Polarizing Plate Beamsplitter PBSW-532, Thorlabs, **L1, 2**: Lens C240TME-A, Thorlabs, **SMF1,2**: Single Mode Fibre P3-488PM-FC-2, Thorlabs, **P**: Linear polarizer LPVISE 100-A, Thorlabs, **L3**: Achromatic Doublet AC254-075-A-ML, Thorlabs, **L4**: Achromatic Doublet AC254-200-A-ML, Thorlabs, **L5, 7**: Achromatic Doublet AC080-010-A-ML, Thorlabs, **L6**: Achromatic Doublet, AC254-080-A-ML, Thorlabs, **DM**: Dichroic Mirror, 540 nm longpass, custom made, **Q1, 2**: Multi-Order Quarter-Wave Plate, WPMQ10M, Thorlabs, **GRIN-MMF**: Graded-Index Multimode Fibre GIF625, Thorlabs, **SI-MMF**: Step-Index Multimode Fibre FG050LGA, Thorlabs, **Obj.**: Objective Olympus Plan N, 20x, 0.40NA, **NPBS**: Non-polarizing Beamsplitter Cube BS016, 50:50, Thorlabs, **L8**: Achromatic Doublet, AC254-150-A-ML, **DMD1, 2**: Digital micro-mirror device V-7001 (DLP 7000, Texas Instruments), ViALUX, **Iris**: Iris diaphragm SM1D12C, Thorlabs, **CMOS**: Camera Ace acA640-750um, Basler.

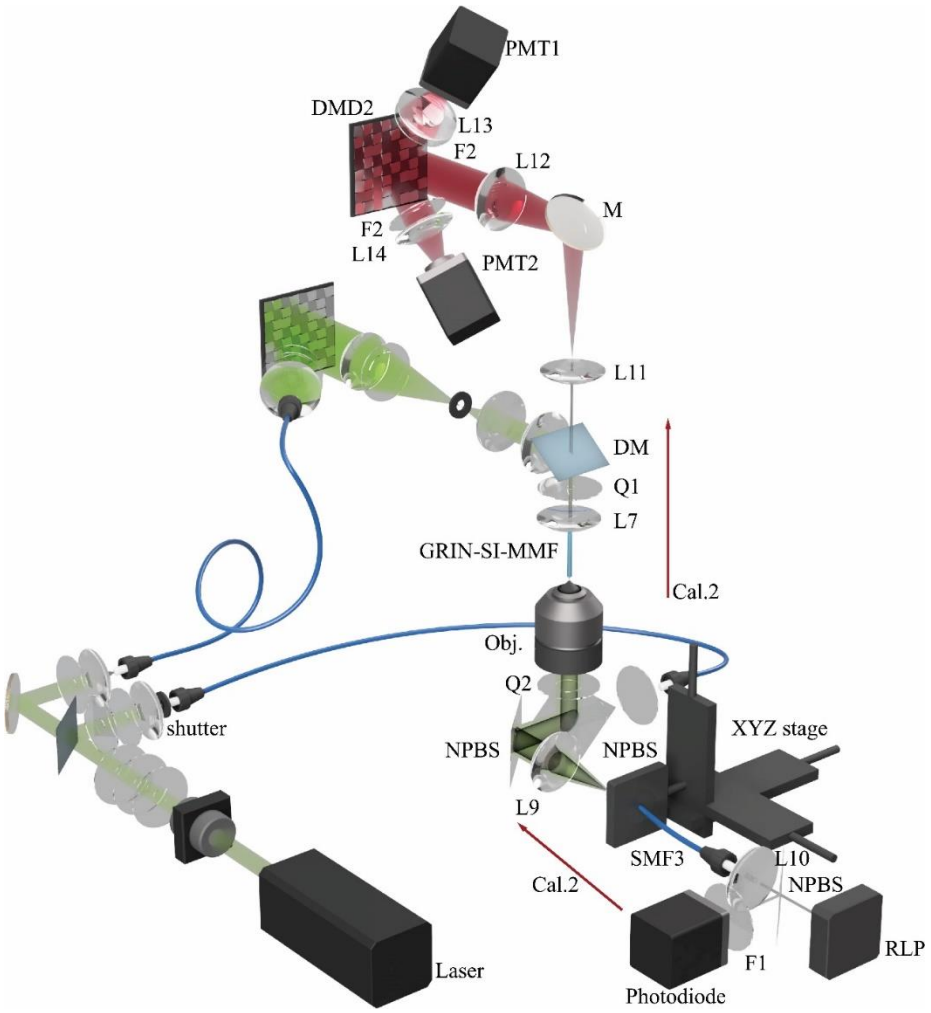

Figure 3.24: A part of the experimental setup intended for the calibration of the annular rings. **L7**: Achromatic Doublet AC080-010-A-ML, Thorlabs, **DM**: Dichroic Mirror, 540 nm longpass, custom made, **Q1, 2**: Multi-Order Quarter-Wave Plate, WPMQ10M, Thorlabs, **GRIN-MMF**: Graded-Index Multimode Fibre GIF625, Thorlabs, **SI-MMF**: Step-Index Multimode Fibre FG050LGA, Thorlabs, **Obj.**: Objective Olympus Plan N, 20x, 0.40NA, **NPBS**: Non-polarizing Beamsplitter Cube BS016, 50:50, Thorlabs, **L9**: Achromatic Doublet AC254-060-A-ML, Thorlabs, **SMF3**: Single Mode Fibre P3-488PM-FC-2, Thorlabs, **F1**: Filter ET525/50, Semrock, **L12**: Achromatic Doublet, AC254-150-A-ML, **L11, 13**: Achromatic Doublet AC254-075-A-ML, Thorlabs, **L14**: Achromatic Doublet, AC254-080-A-ML, Thorlabs, **F2**: Filter FELH0550, Thorlabs, **Laser**: Laser Verdi, G-Series (G5), Coherent, **ISO**: Isolator Tornos Serie 500-1030nm (04-532-00012), **shutter**: Diaphragm shutter with controller, SHB1T, Thorlabs, **DMD2**: Digital micro-mirror device V-7001 (DLP 7000, Texas Instruments), ViALUX, **Iris**: Iris diaphragm SM1D12C, Thorlabs, **RLP**: Red laser pointer 650 nm, **Photodiode**: Photodiode PBW34, Vishay Semiconductors, **PMT**: Photomultiplier Tube PMT2101/M, Thorlabs.

The second part of the setup (Cal.2, Fig. 3.24) is used for the measurement and calibration of annular rings corresponding to scanning focal points within the imaging plane. These rings are used during imaging as confocal masks separating the signal originating from the scanning focal points from the signal excited in the out-of-focal planes. The upper part is used during imaging of the fluorescent sample to detects all the emitted signal or with the confocal masks on the DMD2 to detect a signal with the use of confocal filtration.

The calibration module 2 uses red light from a red laser pointer (RLP) propagating through a non-polarising beamsplitter cube (NPBS) aligned into the SMF3. The outcoming light is focused into the focal plane of the MMF by an objective (Obj.) creating trans-illumination spot. The appropriate location of each red focal spot is determined from an image of the corresponding green calibrated focal spot (coupled into the SMF3) detected on the photodiode. The different positions are generated by scanning

the field of view by a SMF3 fixed to an *x*-*y* stage. The generated red spot mimicking the fluorescent signal emitted purely from the focal spot propagates backward through the GRIN-SI-MMF, DM, and forms a ring on DMD2. The mirrors on DMD2 reflect the signal from within the ring to PMT1. During the sample imaging for every output scanning point, the calculated confocal masks are simultaneously displayed on DMD2, thus reflecting the light only off the micro-mirrors from the confocal ring. It contains the signal only from the scanning points, which is detected on the PMT1. The rest of the signal is reflected outside onto the PMT2.

3.6.3 Calibration procedures of scanning points and confocal masks

In the first calibration step (Fig. 3.23), the transmission matrix (TM) of the system is measured as described in Section 2.5 obtaining a focal point scanning across the whole field of view in the focal plane similar to a scanning microscope. In the second calibration step using the second calibration module (Fig. 3.24), red light from the focal points is back-propagated through the GRIN-SI-MMF and the annular rings formed in the far field of the proximal probe facet are imaged and the confocal masks are calculated.

The calibration is typically carried out for a set of ~110 points distributed in a star-shaped grid across the whole FOV (Fig. 3.25b). For every tested green epi-illumination focal point, a red trans-illumination point is generated by the RLP at the same location in the imaging plane. Red light from this focal point propagates backwards through the GRIN-SI-MMF, forming an annular ring imaged on DMD2. The annular ring is scanned by domains of 8x8 micro-mirrors bins reflecting the signal from the mirrors in the ON position onto the PMT1. From the detected images (Fig.3.25c) a grid with coordinates for fits is estimated map for every detected and measured ring.

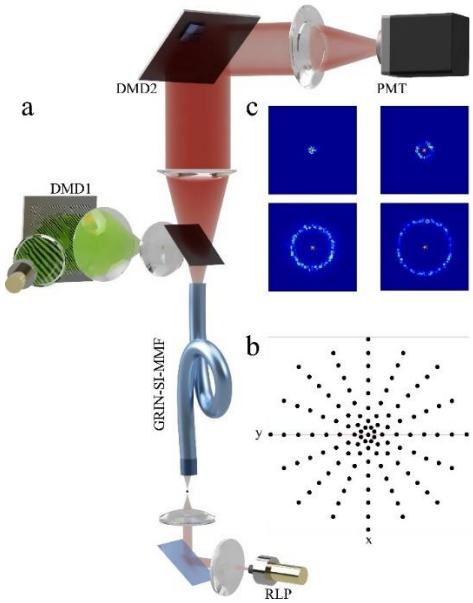

Figure 3.25: A scheme of the calibration procedure. a) Principle of scanning foci in the image plane. b) Organization of the red foci used for calibration of rings on DMD2. c) Detected annular rings on PMT particular to red foci position.

To eliminate the possibility of ring ellipticity on the PMT1 and to obtain masks corresponding to the real shape, as a next step the images for all tested points are fitted with ellipse with the intensity profile I respecting a Gaussian function according to equation

$$I(r) = A \cdot exp\left[-\frac{(r-r_0)^2}{2\sigma^2}\right] + B, \qquad (3.13)$$

where A represents the amplitude of the fit, B is the offset, σ controls the width of the fit and r_0 determines the central radius of the ring. We also fit for the centre of the ring corresponding to the

optical axis of the probe. The measured axes ratio shows that the measured data in this case are more of a ring shape. The Eq. (3.13) is relevant in its form. The measured data serve for calculation of the final thickness, axes ratio and *x-y* centre of the rings. Next, the fitted amplitude *A* is set to 1 and the offset *B* to 0. The confocal masks for the ON mirrors are then calculated as

$$exp\left[-\frac{\left(r-r_{0,M}\right)^2}{2{\sigma_M}^2}\right] \geq CF. \qquad (3.14)$$

The values of σ_M and ring *x-y* centre are calculated as averages of fitted values across all recorded rings. The averages are also used for masks for all scanning points. The radii of masks $r_{0,M}$ for tested points are linearly increasing with increasing radial distance from the probe centre r_F. At the centre x and y, where $r_F = 0$, $r_{0,M} = 0$. All calculated radii $r_{0,M}$ are fitted with a linear function of r_F and radii of all other masks are determined from this fit. The measured ring is interpolated to full DMD2 coordinates. We obtain a final ring with DMD2 resolution, prepared for creation of confocal masks for all output point. The threshold to filter the normalized Gaussian mask is set by a *confocal factor* (CF) defined in an interval <0,1> and yields annular rings with different thicknesses. Therefore, $\mathrm{CF} = 1$ corresponds to maximum signal filtration, $\mathrm{CF} = 0$ corresponds to no filtration of the detected light and. The masks are binarized and used to control DMD2 (Fig. 3.26l): 0 drives the micro-mirrors in the OFF position and 1 in the ON position.Maximum filtration at $\mathrm{CF} = 1$ yields a mask thickness of a single DMD´s micro-mirror in the ON position and minimum filtration $\mathrm{CF} = 0$ a mask with all mirrors ON.

3.6.4 Probe and sample preparation

GRIN-SI-MMF probe

A piece of a SI-MMF of a length ~2-3 cm is right-angle cleaved (Fujikura CT101) and a segment of a GRIN-MMF of length ~2 cm is spliced at the distal facet of the SI-MMF (FG050LGA, Thorlabs, diameter of 125 μm with core diameter of 50 μm and 0.22 NA) by 3SAE Large Diameter Splicing System – LDS 2.5, 3sae Technologies, Inc. The spliced GRIN fibre is right-angle cleaved to length *L* ~220 μm respecting a *P*/4 imaging length in order to achieve a working distance of *d* ~30 μm.

Sample preparation - microspheres

For characterization of the confocal performance of the endoscope a 2D phantom sample was prepared using fluorescent microspheres (diameter of 0.82 μm, Polymer Microsphere, R820, Duke Scientific) dispersed in water (1:1000) dried on a cover glass (0.7 mm thick). A 3D phantom sample was prepared by dispersing fluorescent microspheres (Nile Red, 2.0 μm in dia) in 0.5% agarose gel (Sigma-Aldrich).

3.6.5 Imaging performance of the confocal holographic endoscope

The working distance *d* of the GRIN-SI MMF and the focal plane for different confocal factors should be identical.

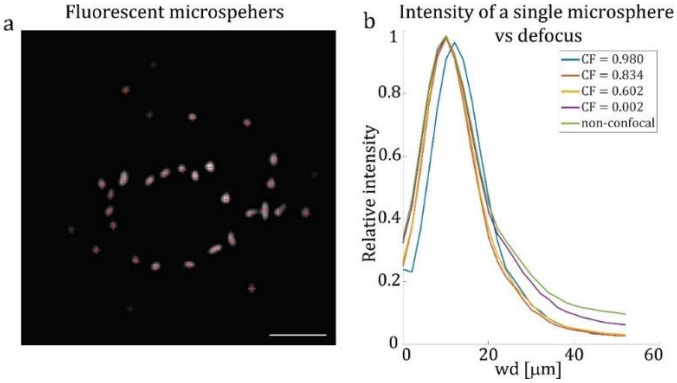

Figure 3.26: Verification of the calibrated working distance. a) Fluorescent microspheres (dia 0.82 μm) on a coverslip imaged at a working distance (wd) of 24 μm. Each image was filtered and individual microspheres were

detected by PMT. Scale bar is 10 μm. b) Normalized intensity at different working distances separated by 2-μm. The intensity was calculated as an average across all microspheres and distinguished as a single object.

We confirmed this by imaging of fluorescent microspheres on a cover slip in a z-stack using 5 different CFs (Fig. 3.26). Figure 3.26b shows the average intensity across all fluorescent microspheres (red cross in Fig. 3.26a) at different working distances. The peak of the intensity determines the position with the sharpest focus – the appropriate working distance. The intensity profiles for CFs 0-0.834 peak at $d = \sim 24$ μm from the distal facet. Then, TM is measured for a new working distance. CF = 0.98 has not been used in experiments.

Single-photon PSF characterization for the confocal endo-microscopy

To determine the quality of the imaging, we first characterized the 3D point spread function (PSF) of the confocal endo-microscopy imaging process and compared it to the corresponding non-confocal PSF (Fig. 3.27). We illuminated a sub-resolution sized fluorescent microsphere (0.82 μm in dia) with a single focal spot and scanned the microsphere in 3D while three different CFs were applied. Figure 3.27 shows the x-y scans of 3 different focal points positioned in the middle (a), at $0.8r$ (b) and 0.4r (c) from the centre (r is the radius of the FOV ~ 25 μm).

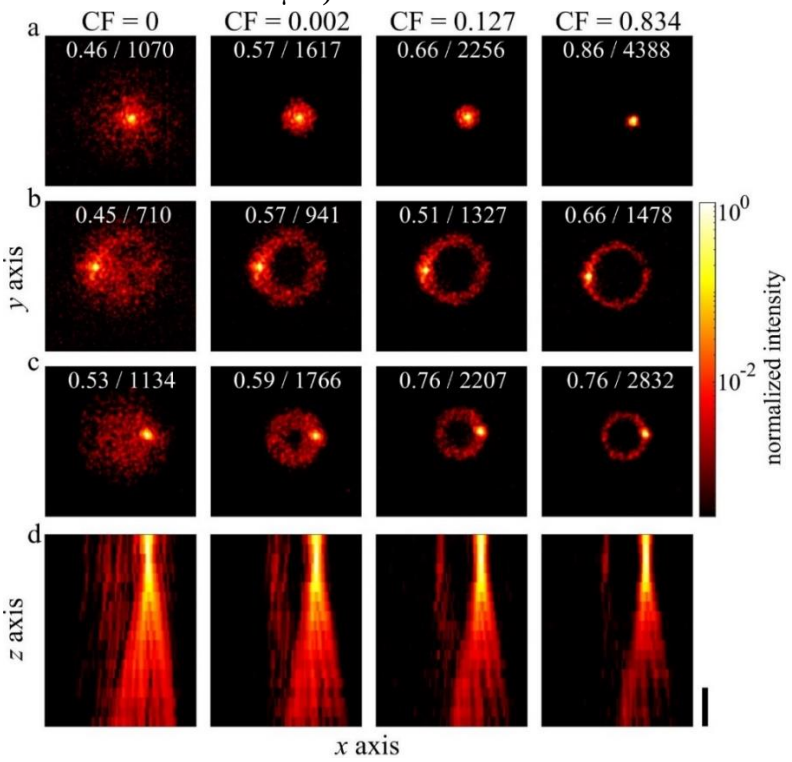

Figure 3.27: 3D PSF of the holographic endoscope with different extent of light filtration. a)-c) Lateral point spread functions (PSF) measured using a sub-resolution fluorescent microsphere (dia 0.82 μm) for three different focal points in the regime of non-confocal imaging CF = 0 and using three different confocal factors (CF = 0.002, 0.127, 0.834). Each image features values of the effective power ratio (EPR) and effective enhancement factor (EEF). Increasing the CF clearly attenuates the speckled background. d) An axial PSF for the focal point in (c) as a sum of intensities across *x-y* plane. The higher CF the stronger out-of-focus light attenuation which is visible also along the optical axis z. Scale bar is 20 μm.

The intensity was detected without confocal filtering ($CF = 0$) and with 3 different confocal factors $CF = 0.002$, 0.127 and 0.834 corresponding to rings with a thickness of 56, 32 and 9 micro-mirrors, respectively. The results demonstrate two confocal effects. Firstly, increasing the CF leads to a significant attenuation of background in the focal plane which is reflected in the increase of the effective enhancement factor (EEF) and effective power ratio (EPR). The EEF is defined as the ratio of peak

intensity at the focal point to the average level of speckled background and the EPR represents the power deposited in the focal spot relative to the total power in the focal plane [95].

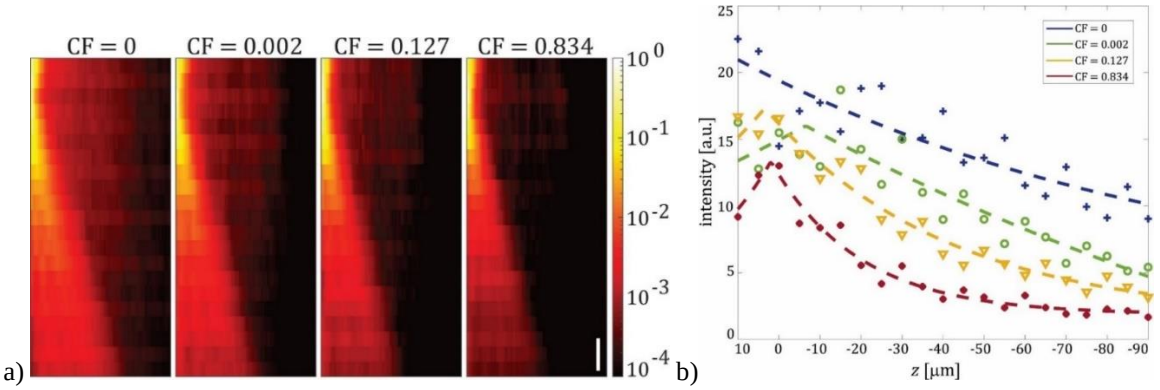

Figure 3.28: a) Azimuthally-averaged intensity profiles of the PSF in the axial plane. Scale bar is 10 μm. b) Total intensity in different planes along the optical axis *z* without confocaling and for tested CFs. The measured values are fitted by Laplace function and the fit is rendered as dashed lines. Positive values of *z* are towards the fibre facet and negative values are in direction away from it.

Since the PSF changes across the field of view, the EEF and EPR enhancements were measured for three radially different positions of the focal spot. The EEF for the selected foci applying CF = 0.834 increase by 310 (a), 108 (b) and 150 % (c), respectively. Using the same CF, the EPR values increase by 80 (a), 46 (b) and 43 % (c), respectively. Second "confocal" effect is a significant attenuation of light from the out-of-focus planes which can be seen from the *x*-*z* projections in Fig. 3.27d, where the points in *x* are a sum of intensities along the *y* axis, for each *x*-*y* plane. Figure 3.28a) demonstrates further the attenuation in the axial intensity averaged across the azimuth. The suppression of the out-of-focus light is also demonstrated in Figure 3.28b).

Volumetric imaging of a phantom sample

To verify the results of previous measurement, we tested the imaging performance in a 3D model sample of fluorescent microspheres (2 μm in dia) dispersed in an agarose gel 1:1000. Figure 3.29 shows two example FOVs, where the out-of-focus light is clearly attenuated after confocal filtration leading to decrease of the background intensity and increase of image contrast.

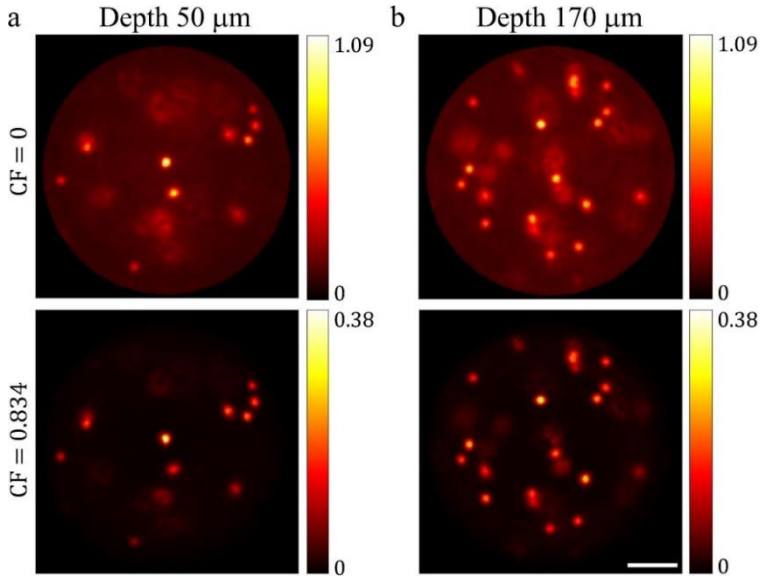

Figure 3.29: Imaging of a 3D model sample of fluorescent microspheres (dia 0.82 μm) dispersed in agar at depth 50 μm (a) and 170 μm (b). Confocal filtration leads to attenuation of the out-of-focus light. Scale bar is 10 μm.

Preparation of the tissue sample for testing the confocal imaging

Moving towards real experimental conditions, we tested holographic confocal micro-endoscopy in imaging of fixed mouse brain slices. A transgenic mouse line with a tdTomato expressed in excitatory neurons was generated as described in Section 3.5.1. The brains were extracted and fixed as described in Section 3.5.2.

Confocal endo-microscopy of fixed brain slices

We calibrated the confocal masks for $CF = 0.834$. Figure 3.30 shows the comparison of non-confocal ($CF=0$, top row) and confocal images ($CF=0.834$, bottom row) of excitatory neurons. The out-of-focus fluorescence signal is clearly attenuated in the confocal images and thus we can distinguish somas of the neurons in the focal plane (Fig. 3.30b).

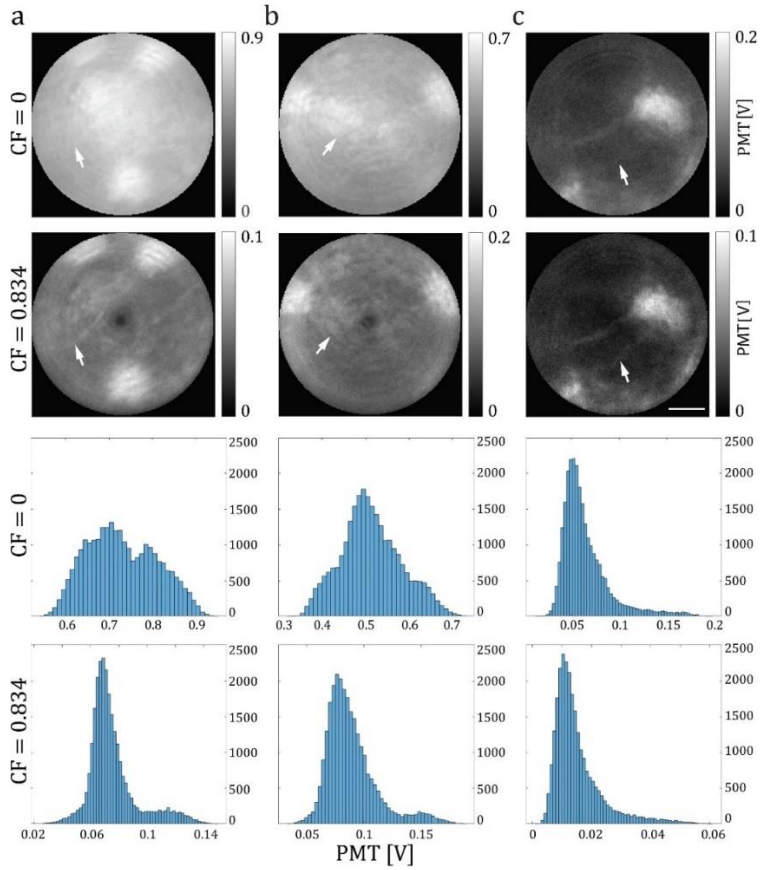

Figure 3.30: Imaging of neurons expressing tdTomato in fixed brain slices. Three different fields of view (a, b, c) imaged with $CF = 0$ (top) and $CF = 0.834$ (bottom) and corresponding histograms of their intensities. a), c) A neuronal process emerged after confocal attenuation of the background. b) A putative soma disappeared after attenuation of light from out-of-focus planes. Scale bar is 10 μm.

The background of the images is reduced increasing the contrast of the images, i.e. yields higher signal to background ratio. A thin neuronal processes not resolved in the non-confocal images (Fig. 3.30a, c image) can be detected. The effect of the confocal filtration is quantitatively demonstrated in histograms with distributed intensities from corresponding images above. For the non-confocal imaging (CF=0) in cases Fig. 3.30a and b, the contrast is low and the neuronal somas are not distinguishable. This can also be expected from the corresponding histogram – its width signalizes a low image contrast and a high amount of background signal and out-of-focus signal. However, after applying confocal filtration using CF = 0.834 the histogram is visibly narrower.

3.6.6 Imaging performance of the confocal holographic endoscope using a side-view probe

During imaging with the MMF *en face*, a moving probe results in mechanical tear of the tissue damaging especially the cells of interest. In our group we have developed a side-view probe developed

and applied for *ex-vivo* and *in-vivo* imaging [106, 107]. The focal plane is formed off-axis along the longitudinal axis of the fibre (Fig. 3.31). This significantly decreases the displacement of the tissue when moving the probe. The GRIN-SI-MMF side-view probes prepared by polishing fibre facet to the 45° and coated with aluminium.

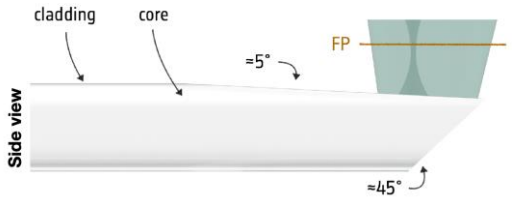

Figure 3.31: Schematic illustration of the novel side-view MMF imaging probe, with indication of the angles of the polished surfaces and focal plane (FP). For a side-view imaging, the light propagates along the fibre core and at the end is internally reflected on a 45°-polished surface with a reflective coating, leaving the fibre through the flat 5°-polished output facet and is focused on FP at the distance set during a calibration procedure. Reprinted from [106].

Single-photon PSF characterization for the confocal endo-microscopy using a side-view GRIN-SI-MMF probe

We have measure the PSF of the side-view probe without confocal filtration ($CF = 0$) and using confocal factor $CF = 0.867$ (8 micro-mirrors) in a similar manner to the straight-view mode presented in Section 3.6.5 with fluorescent microsphere (0.82 μm in dia).

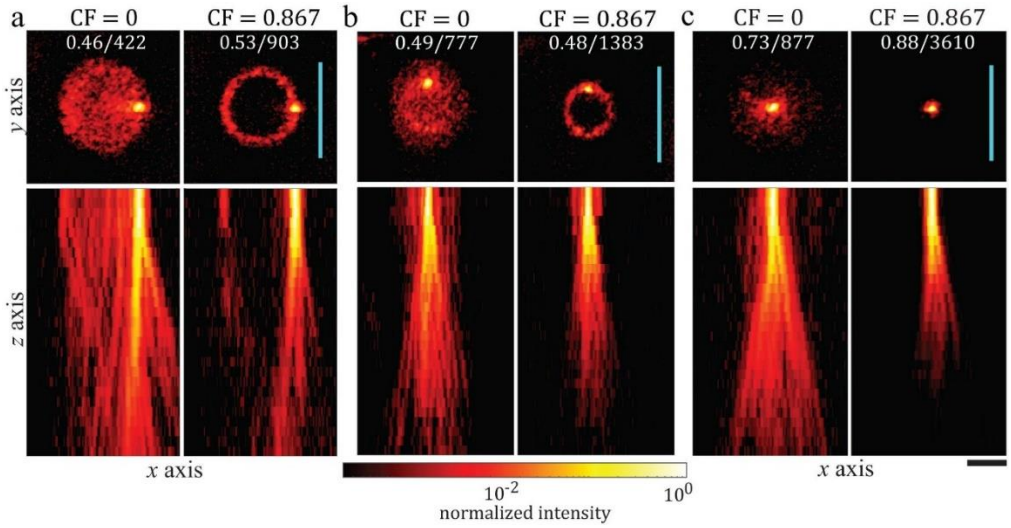

Figure 3.32: 3D PSF of the holographic endoscope with different extent of light filtration in the side-view mode. a-c, Lateral point spread functions (PSF) measured using a sub-resolution fluorescent microsphere (dia 0.82 μm) for three different focal points (top) and axial PSF for each focal point (bottom). Each point is imaged without confocal filtering and with a CF = 0.867. The values of EPR/EEF are given for each focal point. The blue lines mark the edge of the FOV of the MMF´s distal end. Scale bar is 20 μm.

Figure 3.32 show *x*-*y* scans of three different focal points at $0.8r$ (a), $0.4r$ (b) and in the middle (c) of the FOV, where *r* is the radius of the FOV (~25 μm). Confocal filtration leads to a significant attenuation of background in the focal plane reflected in the increase of EEF and EPR. The EEF for the selected foci and $CF = 0.867$ shown in Fig. 3.32 increase from the left by 315, 78 and 114%, respectively. EPR values increase by 20% in a) and 15 % in c), while for case b) there has been decrease by 2%. Even though, the light attenuation outside the focus is still fully apparent. A significant attenuation of light from the out-of-focus planes also can be clearly seen from the *x*-*z* projections in bottom panels of Fig. 3.32, where the points in *x* are a sum of intensities along the *y* axis, for each *x*-*y* plane and the azimuthal averages shown in Fig. 3.33. The confocal effect is also demonstrated in Figure

3.34. The more the focal point is radially to the centre of the FOV, the stronger the confocal effect can be observed.

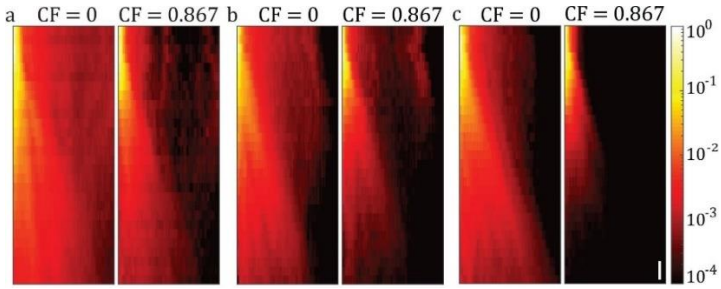

Figure 3.33: Azimuthally-averaged intensity profiles of the PSFs in the axial plane for focal points at three different positions in the FOV (a-c). Scale bar is 10 μm.

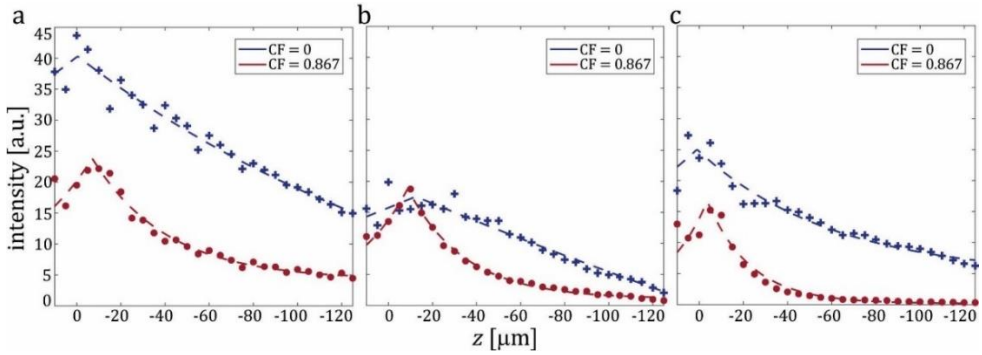

Figure 3.34: Total intensity in different planes along the optical axis *z* without confocal filtration and for the tested CF. The measured values of focal points at three different positions: 0.8*r* (a), 0.4*r* (b) and in the middle (c) are fitted by Laplace function and the fits are rendered as dashed lines. Negative values of *x* refer to direction away from the fibre facet.

Confocal imaging of a phantom sample in the side-view mode

To verify the effect of light attenuation we tested the imaging performance in a 3D model sample - fluorescent microspheres (0.82 μm in dia) in an agarose gel (1:1000, Fig. 3.35). We can see that the out-of-focus light is clearly attenuated after confocal filtration.

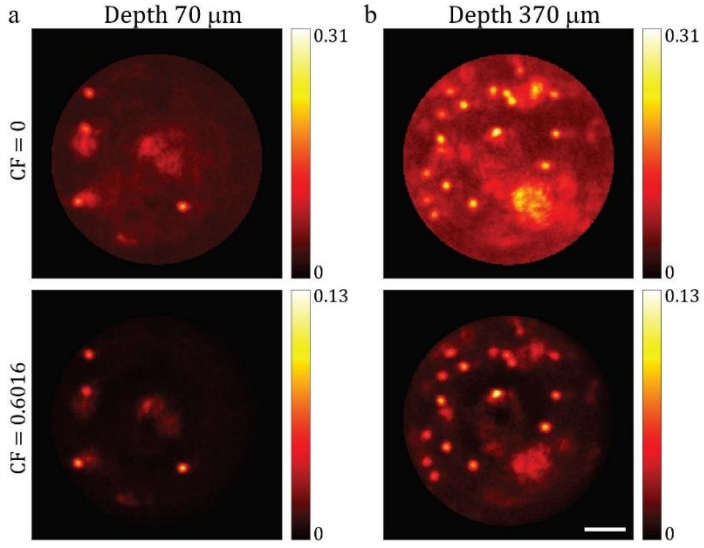

Figure 3.35: Side-view imaging of a 3D model sample of fluorescent microspheres (dia 0.82 μm) dispersed in agar at depth 70 μm (a) and 370 μm (b). Confocal filtration leads to attenuation of the out-of-focus light. Scale bar is 10 μm.

4. Discussion and conclusions

Our first goal was building a holographic endoscope setup following previous work of [103] and bring it to routine high-resolution imaging of biological tissue. Our first main challenge was the stability of the imaging, which can be defined by the quality of the scanning focal point determined by the percentage representation of the total power in such calibrated spot. The major aspect affecting stability turned out to be temperature changes which have a strong impact on the DMD chip. During scanning the DMD chip is warming up and gets deformed. This results in deforming the modulated wavefront, which leads to a different layout of the output light due to the changed phase shifts of the ones measured in TM. This problem was solved by adding a thermoelectric cooler (TEC) with a Peltier chip and a heat sink at the back of the DMD. It works as a thermoregulator with feedback. The temperature changes also strongly affect the polarisation in single mode fibre. It was stabilized by adding a polariser plate at the output of the SMF2 before the beam reaches the DMD chip. This enabled to fully control the polarisation of the coherent beam. With these modifications we reached a stability of the focal spot for 50 hours with only minor changes of the power ratio.

The stability of the system was tested on imaging of fluorescent microspheres both in 2D and 3D. In order to refocus in the sample, the user can either move the probe with respect to the tissue or refocus the scanning spot. We implemented here refocusing by acquisition of the TM at different working distances from the distal fibre facet. This allowed us volumetric imaging and focusing closer to the objects of interest. This is important particularly for *in vivo* imaging, where moving of the probe disrupts the tissue and displaces the cells of interest.

In order to enhance the capacity of the endoscope for high-resolution imaging, we proposed two computational algorithms for image post-processing that enhance it's contrast and thus the resolution. In this approach, the sample is reconstructed using measurement of the spatial intensity profiles of all focal points with their speckled background - the "muddy modes" and records of the sample image. One of the presented algorithms implements a regularised iterative inversion and the second algorithm employs a direct pseudo-inversion calculated by a singular value decomposition (SVD). The iterative algorithm called here the PN-based method represents a "more correct" model since it respects the Poisson noise distribution in the image, and it relies on an iterative calculation of a set of equations for every single image. The pseudo-inversion, called here the IIN-based method, on the other hand does not respect Poisson distribution of noise in images. However, it allows to use a simple last-square minimization assuming the Gaussian type of noise with constant variance. Thus, the solution can be calculated using the SVD which constitutes a simple vector-matrix multiplication for every image. Both methods were regularised using the Tikhonov regularisation with the regulariser strength λ. Enhancement of different spatial frequencies depend directly on λ. Both methods yield images with increased contrast for all spatial frequencies present in the image, evaluated using an USAF target sample.

Using the PN-based method, the contrast of all analysed spatial frequencies in our sample can be enhanced by up to $> 68\%$. Moreover, all spatial frequencies reach the maximum contrast within the same interval $1.5 \times 10^{-6} \leq \lambda \leq 5 \times 10^{-6}$. The PSNR and SSIM metrics reporting image quality in the fidelity of the reconstructed image to the "ground truth" and the visual impact of luminance, contrast and structure can be enhanced up to 14% and 29% respectively. Importantly, the regularised PN-based inversion yields a wide interval of $\lambda < 6 \times 10^{-5}$, for which all three image quality criteria are enhanced. Selecting a λ from this range allows fine-tuning of the image quality towards maximum contrast enhancement or PSNR and SSIM, respectively. The reconstruction of a single frame with this method takes ~ 21 seconds using a computational server equipped with 4 Intel Xeon Gold 6126 CPUs.

In the IIN-based inversion, the enhancement of image quality is given also by λ but its range is additionally limited by the presence of negative values in the reconstructions. We set a limit on λ accepting a maximum 1% of image pixels being negative. Therefore, the transformation yields enhanced image quality in a narrow interval $0.16 \leq \lambda \leq 0.18$. The contrast of all frequencies can be

enhanced up to at least 69%, which is comparable to the PN-based inversion. Both PSNR as well as SSIM are enhanced in the same interval of λ by maximum of 10% and 26%, respectively as compared to 14% and 29% in the case of the PN-based inversion. Although the IIN-based method does not use the correct model for noise, it can be calculated as a pseudo-inverse using SVD which constitutes a simple vector-matrix multiplication for every image. The initial computation of matrix $\mathbf{M}+'$ in the regularized SVD procedure takes 15 minutes using the same computational power. The reconstruction of every additional frame however takes only $\sim$0.2 seconds which can be highly advantageous in reconstructions of videos with fast feedback.

We also demonstrated that λ derived from one image can be successfully applied to the reconstruction of a series of images of a changing FOV from the same as well as different sample. (PN and IIN in Fig. 3.18 and in Visualization1).

The performance of PN and IIN-based reconstruction algorithms is dependent on the level of detected photons. Therefore, the methods and their comparison cannot be considered universal. The presented results were obtained with a photon count typically in a range 2000 in a single muddy mode. With decreasing signal to noise, the iterative algorithm is likely to become more advantageous yielding better results while the direct inversion will tend to amplify the noise in the SVD process.

Finally, the presented methods have been meant to be applied for image enhancement of biological specimens, however the presented form in this work is limited only to planar (2D) samples. Nevertheless, the concepts can be extended to the third dimension paving the way to reconstructions of volume samples such as tissue *in vivo*.

Considering the limitations of 1-photon fluorescence imaging I was looking for a suitable animal model for brain imaging (Section 3.5.1). This presumes bright fluorescent indicators and sparse labeling of cells in the dense brain tissue. Limited by the regulations of our animal facility we opted for crossbreeding of mouse lines in the Cre-lox breeding system which enable to express the selected fluorescent protein in a specific cell type. By cross-breading of a transgenic mouse line B6.Cg-*Gt(ROSA)26Sor*$^{tm14(CAG\text{-}tdTomato)Hze}$/J and Cre-recombinase-expressing mouse line B6;129S6-Tg(Camk2a-cre/ERT2)1Aibs/J we obtained offsprings with tdTomato expressed in excitatory neurons. Additionally, we limited the fluorescence expression by injection of tamoxifen (Section 3.5.1.). Endoscopic imaging of fixed brain slices of this tissue showed however that the density is still quite high, and the contrast of images is not satisfactory (Section 3.5.3.).

This has led the motivation to upgrade the technology in order to limit the out-of-focus signal.

The proposed method relies confocal filtration of light using a novel probe of a GRIN-MMF spliced on a SI-MMF. This probe images light coming from a focal point into a defined annular ring in the far field of the proximal fibre facet [53]. Light coming from radially different positions appear outside of this ring and can therefore be separated. Light coming from axially different positions will appear defocused in the far field and its contribution to the detected signal can therefore be minimized. We used a second DMD and applied confocal ring masks in order to filter the light. The thickness of the ring-mask displayed on DMD2 determines the extent of signal filtration and we call it here the "confocal factor (CF)". A higher CF corresponds to a thinner ring-mask facilitating stronger light filtration, similarly to a confocal pinhole in classical far-field laser scanning confocal microscopy (CLSM).

As a proof of concept, we have imaged sub-resolution fluorescence microspheres and demonstrated that the presented confocal filtering of signal leads to a significant attenuation of the out-of-focus light both in the focal plane and also axially. This was quantified by the effective enhancement factor (EEF) and effective power ratio (EPR) reaching up to 310% and 80% (Fig. 3.27). The actual EEF and EPR values for the wide-field PSF are somewhat lower than was previously reported [103]. The lower values can be attributed to the fact, that it was measured using fluorescent microspheres rather than the focal point illumination directly.

The confocal effects were also demonstrated in imaging of a 3D sample of fluorescent microspheres dispersed in agar. The background signal and signal from outside the focal plane is successfully

attenuated (Fig. 3.29). Importantly the confocal effect has been demonstrated by *ex vivo* imaging of brain slices expressing tdTomato in a population of excitatory neurons (Fig. 3.30). Also here, the background signal is clearly attenuated, which leads to an increase of image contrast and thus resolution manifested by the emergence of thin neuronal processes (Fig. 3.30a and c). The attenuation of the out-of-focus signal shows e.g. as the vanishing of a putative cell body (Fig. 3.30b).

Comparing with classical confocal microscopy which de-scans the pinhole for every *x, y* position, our filtration works only in a single dimension in polar coordinates. This means that light coming from azimuthally different positions but the same radius from the centre will share the same ring-mask. As a consequence, the detected signal from a single focal point at a radial distance *r* will be contaminated by the background signal coming from a ring with the same radius (Fig. 3.27b and c).

The parameters of masks are optimised for signal detection from the focal plane. Annular rings of the same thickness given by the CF, decrease the central diameter for focal points with decreasing radial distance in the focal plane down to an experimentally measured minimum radius. The signal intensity coming from axially different planes however is modulated by the area of the masks which is decreasing towards the middle. Scanning points with a decreasing radial distance in the focal plane correspond to annular ring masks with a decreasing radius. Decreasing the mask radius more than the theoretical resolution limit will lead to a decrease in the detected intensity of the corresponding central points. In practice, the intensity-decrease artifact appears even for a mask of a bigger diameter. Therefore, we measured the minimum mask diameter experimentally aiming for zero intensity drop in the centre of an image of a 2D homogeneous sample. This is why we can sometimes see an intensity dip in the middle of confocal images of 3D samples (Fig. 3.30a, b). Similarly, to classical CLSM, the amount of detected photons in the confocal endo-microscopy is decreased due to the filtration process. Using the maximal CF, we can lose approximately more than 50% of the total light compared to non-confocal imaging (Fig. 3.29b) It is typically compensated for by increasing illumination intensity, paying attention not to cause photobleaching. As the next goal we aimed at implementing this confocal principle through the side-view probes which are to be used in imaging *in vivo*. We tested again the suppression of signal by scanning a sub-resolution fluorescence microsphere which revealed a significant increase of the effective enhancement factor (EEF) and effective power ratio (EPR) by up to 314% and 20%, respectively (Fig. 3.32) within the focal plane. Also the light from out-of-focus planes is clearly attenuated (Figures 3.32b, 3.33 and 3.34). These effects were also demonstrated in imaging of a 3D sample of fluorescent microspheres dispersed in agar (Fig. 3.35).

All the confocal experiments were carried out with step index and graded-index MMFs with a low NA of 0.22 and 0.275 and core diameters of 50 μm and 62.5 μm, respectively. Although the effects of confocal filtration are already undisputable, they are expected to be much more pronounced using fibres with higher NA and bigger core. As in the classical CLSM, confocal holographic endo-microscopy will open the door for imaging samples with a denser expression of fluorescent indicators. Thus, it increases the number of imaged cells per unit of time. In functional imaging, such as intracellular calcium, it will facilitate easier detection of spikes from individual cells due to decreased crosstalk from neuropil and other cells. Therefore, the next step, as a continuation of this work, is to apply this novel probe in vivo for imaging deep in the brain tissue. A small form factor of the probe promises funnelling confocal fluorescence imaging to unprecedented depth in a minimally invasive manner. This work has brought a strong base and new knowledge for a further shift towards *in-vivo* imaging of brain tissue in a living animal.

To conclude my work, we are equipped now with an ultra-thin endoscope setup which is capable of stable imaging of fluorescent samples in the range of hours featuring the possibility to refocus within the sample without moving the probe. The acquired imaging can be further enhanced via computational post-processing. Moreover, this setup has been enriched by a confocal module which allows to significantly attenuate the out-of-focus light and is therefore much more suitable for imaging in the dense brain tissue.

References

[1] Waterson, R.H., Lindblad-Toh, K., Birney, E., Rogers, J., Abril, J.F., Agarwal, P. et al. Initial sequencing and comparative analysis of the mouse genome. Nature, 420(6915): 520-62, 2002. https://doi.org/10.1038/nature01262. [2] Čižmár, T. Exploiting multimode waveguides for in vivo imaging, SPIE, 2015.

[3] Suzuki, T., Matsuzaki, T., Hagiwara, H., Aoki, T. and Takata, K. Recent Advances in Fluorescent Labeling Techniques for Fluorescence Microscopy. *Acta Histochem Cytochem*, 40(5), 2007. https://doi.org/10.1267/ahc.07023.

[4] Latychevskaia T., Lateral and axial resolution criteria in incoherent and coheren optics and holography, near- and far-field regimes. *Applied Optics*, 58(13), 2019. http://doi.org/ 10.1364/AO.58.003597

[5] Helmchen, F. Denk, W. Deep tissue two-photon microscopy. *Nature Methods*, 2: 932-940, 2005. http://doi.org/ 10.1038/NMETH818.

[6] Yaroslavsky, A.N., Schulze, P.C., Yaroslavsky, I.V., Schober, R., Ulrich, F. and Schwarzmaier, H.-J. Optical properties of selected native and coagulated human brain tissues *in vitro* in the visible and near infrared spectral range. *Physics in Medicine & Biology* 47(12), 2002. http://doi.org/10.1088/0031-9155/47/12/305.

[7] Kleinfeld, D., Mitra, P.P., Helmchen, F. and Denk, W. Fluctuations and stimulus-induced changes in blood flow observed in individual capillaries in layers 2 through 4 of rat neocortex. *Proceedings of the National Academy of Sciences*, 95(26), 1998. https://doi.org/10.1073/pnas.95.26.15741.

[8] Oheim, M., Beaurepaire, E., Chaigneau, E., Mertz, J., Charpak, S. Two-photon microscopy in brain tissue: parameters influencing the imaging depth. *Journal of Neuroscience Methods*, 111(1), 2001. https://doi.org/10.1016/s0165-0270(01)00438-1.

[9] Booth, M.J. and Wilson T. Refractive-index-mismatch induced aberrations in single-photon and two-photon microscopy and the use of aberration correction. *Journal of Biomedical Optics*, 6(3), 2001. https://doi.org/10.1117/1.1382808.

[10] Brakenhoff, G.J., Van der Voort, H.T., Van Sprosen, E.A., Linnemans, W.A. and Nanninga, N. Three-dimensional chromatin distribution in neuroblastoma nuclei shown by confocal scanning laser microscopy. *Nature*, 317(6039), 1985. https://doi.org/10.1038/317748a0.

[11] White, J.G., Amos, W.B. and Fordham, M. An evaluation of confocal versus conventional imaging of biological structures by fluorescence light microscopy. *The Journal of Cell Biology*, 105(1):41-48, 1987. https://doi.org/ 10.1083/jcb.105.1.41.

[12] Pawley, J.B. Handbook of Biological Confocal Microscopy. Third edition, Springer Science & Business Media, LLC, New York. 2006.

[13] Wilson, T. and Sheppard C. Theory and Practice of Scanning Optical Microscopy. Academic Press INC. London, ISBN 0-12-757760-2 LCCCN 83-73235, 1984.

[14] Ntziachristos V. Going deeper than microscopy: the optical imaging frontier in biology. *Nature Methods*, 7(8): 603-14, 2010. https://doi.org/10.1038/nmeth.1483.

[15] Fouquet C., Gilles J.F., Heck N., Dos Santos M., Schwartzmann R., Cannaya V., Morel, M.-P., Davidson, R.S., Trembleau, A. and Bolte, S. Improving Axial Resolution in Confocal Microscopy with New High Refractive Index Mounting Media. *PLoS ONE*, 10(3): e0121096, 2015. https://doi.org/10.1371/journal. pone.0121096.

[16] Schermelleh L., Heintzmann R. and Leonhardt H. A guide to super-resolution fluorescence microscopy, *The Journal of Cell Biology*, 190(2), 165–175, 2010. https://doi.org/10.1083/jcb.201002018.

[17] Centonze V.E. and White J.G. Multiphoton Excitation Provides Optical Sections from Deeper within Scattering Specimens than Confocal Imaging. *Biophysical Journal*, 75: 2015-2024, 1998. https://doi.org/10.1016/S0006-3495(98)77643-X.

[18] Sadegh, S., Yang, M.H., Ferri, Ch.G.L., Thunemann, M., Saisan, P.A., Wei, Z., Rodriguez, E.A., Adams, S.R., Kilic, K., Boas, D.A., Devor A. and Fainman, Y. efficient non-degenerate two-photon excitation for fluorescence microscopy. Optics Express, 27(20): 28022-28035, 2019. https://doi.org/10.1364/OE.27.028022.

[19] Helmchen, F. Two-Photon Functional Imaging of Neuronal Activity. *In Vivo Optical Imaging of Brain Function*, second edition, Boca Raton, Frosting RD, editor (2009).

[20] Tsai, P.S. and Kleinfeld, D. In Vivo Two-Photon Laser Scanning Microscopy with Concurrent Plasma-Mediated Ablation Principles and Hardware Realization. *In In Vivo optical Imaging of Brain Function*. CRC Press/Taylor and Francis. ISBN-13: 978-1-4200-7684-4 Second edition. 2009.

[21] Zipfel, W.R., Williams, R.M. and Webb, W.W. Nonlinear magic: multiphoton microscopy in the biosciences. *Nature Biotechnology*, 21(11), 2003. https://doi.org/ 10.1038/nbt899

[22] Hillman E.M.C. Optical brain imaging *in vivo*: techniques and applications from animal to man. *Journal of Biomedical Optics*, 12(5), 051402, 2007. https://doi.org/10.1117/1.2789693.

[23] Kobat D., Horton, N.G. and Xu Ch. *In vivo* two-photon microscopy to 1.6-mm depth in mouse cortex. *Journal of Biomedical Optics*, 16(10), 106014, 2011. https://doi.org/10.1117/1.3646209.

[24] Horton N.G., Wang, K., Kobat, D., Clerk, C.G., Wise, F.W., Schaffer, Ch.B. and Xu Ch. In vivo three-photon microscopy of subcortical structures within an intact mouse brain. Nature Photonics, 7(3): 205-209, 2013. https://doi.org/10.1038/nphoton.2012.336.

[25] Liu, H., Zhuang, Z., He, J., Tong, S., He, Ch., Deng, X., Song, G., Qiu, P. and Wang, K. High-energy polarized soliton synthesis and its application to deep-brain 3-photon microscopy in vivo. *Optics Express*, 27(11): 15309-15317, 2019. https://doi.org/10.1364/OE.27.015309.

[26] Chen, X., Cheng, H., Deng, X., Tong, S., Li, J., Qiu, P. and Wang, K. Self-phase-modulated femtosecond laser source at 1603 nm and its application to deep-brain 3-photon microscopy in vivo. *Journal Of Biophotonics*, 2020, https://doi.org/10.1002/jbio.202000349.

[27] Dombeck D.A., Harvey Ch.D., Tian L., Looger L.L., Tank D.W. Functional imaging of hippocampal place cells at cellular resolution during virtual navigation. *Natural Neuroscience*, 13(11), 2010. https://doi.org/10.1038/nn.2648.

[28] Vaidya, A.R., Pujara, M.S., Petrides, M., Murray, E.A. and Fellowe, L.K. Lesion studies in contemporary neuroscience. Trends of Cognitive Sciences, 23(8): 653-671, 2019. https://doi.org/10.1016/j.tics.2019.05.009.

[29] Jung, J.C., Mehta, A.D., Aksay, E., Stepnoski, R. and Schnitzer, M.J. In vivo mammalian brain imaging using one-and two-photon fluorescence microendoscopy. *Journal of Neurophysiology*, 92: 3121–3133, 2004. https://doi.org/10.1152/jn.00234.2004.

[30] Murayama, M., Pérez-Garci, E., Nevian, T., Bock, T., Senn, W. and Larkum, M.E. . Dendritic encoding of sensory stimuli controlled by deep cortical interneurons. *Nature*, 457: 1137, 2009. https://doi.org/10.1038/nature07663.

[31] Murayama, M., Pérez-Garci, E., Lüscher, H.-R. and Larkum, M.E. Fiberoptic system for recording dendritic calcium signals in layer 5 neocortical pyramidal cells in freely moving rats. *Journal of Neurophysiology*, 98: 1791–1805, 2007. https://doi.org/10.1152/jn.00082.2007.

[32] Knittel, J., Schnieder, L., G. Buess, Messerschmidt, B. and Possner, T. Endoscope-compatible confocal microscope using a gradient index-lens system. *Optics Communications*, 188(5-6): 267–273, 2001. https://doi.org/10.1016/S0030-4018(00)01164-0.

[33] Gmitro, A.F. and Aziz, D. Confocal microscopy through a fiber-optic imaging bundle. *Optics Letters*, 18(8): 565–567, 1993. https://doi.org/10.1364/OL.18.000565.

[34] Loterie, D., Goorden, S.A., Psaltis, D. and Moser, Ch. Confocal microscopy through a multimode fiber using optical correlation. *Optics Letters*, 40(24): 5754-5757, 2015. https://doi.org/10.1364/OL.40.005754.

[35] Engelbrecht, C.J., Johnston, R.S., Seibel, E.J. and Helmchen, F. Ultra-compact fiber-optic two-photon microscope for functional fluorescence imaging in vivo. *Optics Express*, 16(8): 5556–5564, 2008. https://doi.org/10.1364/OE.16.005556.

[36] Wilt, B.A., Burns, L.D., Wei Ho, E.T., Ghosh, K.K., Mukamel, E.A. and Schnitzer, M.J. Advances in light microscopy for neuroscience. *Annual Review of Neuroscience*, 32:435–506, 2009. https://doi.org/10.1146/annurev.neuro.051508.135540.

[37] Saleh, B.E.A., Teich, M.C. *Fundamentals of Photonics*, second edition, John Wiley & Sons, Inc, 2007, ISBN: 978-0-471-35832-9.

[38] Jung J.C. and Schnitzer M.J. Multiphoton endoscopy. *Optics Letters*, 28(11):902-904, 2003. https://doi.org/10.1364/OL.28.000902.

[39] Antonini, A., Sattin, A., Moroni, M., Bovetti, S., Moretti, C., Succol, F., Forli, A., Vecchia, D., Rajamanickam, V.P., Bertoncini, A., Panzeri, S., Liberale, C. and Fellin, T. Extended field-of-view ultrathin microendoscopes for high-resolution two-photon imaging with minimal invasiveness, *eLife*, 9:e58882, 2020. https://doi.org/10.7554/eLife.58882.

[40] Barretto R.P.J. and Schnitzer M.J. In vivo Optical Microendoscopy for Imaging Cells Lying Deep within Live Tissue. *Cold Spring Harb Protocols*, 2012(10): 1029-1034, 2012. https://doi.org/10.1101/pdb.top071464.

[41] Levene, M.J., Dombeck, D.A., Kasischke, K.A., Molloy, R.P. and Webb, W.W. In vivo multiphoton microscopy of deep brain tissue. *Journal of Neurophysiology*, 91(4): 1908-1912 (2004). https://doi.org/10.1152/jn.01007.2003.

[42] Huland, D.M., Brown, C.M., Howard, S.S., Ouzounov D.G., Pavlova, I., Wang, K., Rivera, D.R., Webb, W.W. and Xu, Ch. In vivo imaging of unstained tissues using long gradient index lens multiphoton endoscopic systems. *Biomedical Optics Express*, 3(5): 1077–1085, 2012. https://doi.org/10.1364/BOE.3.001077.

[43] Huland, D.M., Charan, K., Ouzounov D.G., Jones, J.S., Nishimura, N. and Xu, Ch. Three-photon excited fluorescence imaging of unstained tissue using a GRIN lens endoscope. *Biomedical Optics Express*, 4(5): 652-658, 2013. https://doi.org/10.1364/BOE.4.000652.

[44] Chien, Y.-F., Lin, J.-Y., Yeh, P.-T., Hsu, K.J., Tsai, Y.-H., Chen, S.-K. and Chu, S.-W. Dual Grin lens two-photon endoscopy for high-speed volumetric and deep brain imaging. Biomedical Optics Express, 12(1): 162-172, 2021. https://doi.org/10.1364/BOE.405738.

[45] Llewellyn M.E., Barretto R.P.J., Delp S.L. and Schnitzer M.J. Minimally invasive high-speed imaging of sarcomere contractile dynamics in mice and humans. *Nature*, 454(7205): 784-788, 2008. https://doi.org/10.1038/nature07104.

[46] Leiner, D.C. and Prescott, R. Correction of chromatic aberrations in GRIN endoscopes. *Applied Optics*, 22(3): 383-386, 1983. https://doi.org/10.1364/AO.22.000383.

[47] Bortoletto, F., Bonoli, C., Panizzolo, P., Ciubotaru, C.D., and Mammano, F. Multiphoton Fluorescence Microscopy with GRIN Objective Aberration Correction by Low Order Adaptive Optics. *PLoS ONE*, 6(7): e22321 (2011). https://doi.org/ 10.1371/journal.pone.0022321.

[48] W. M. Lee, W.M. and S. H. Yun, S.H. Adaptive aberration correction of GRIN lenses for confocal endomicroscopy. *Optics Letters*, 36(23): 4608-4610, 2011. https://doi.org/10.1364/OL.36.004608.

[49] Wang Ch. and Ji N. Pupil-segmentation-based adaptive optical correction of a high-numerical-aperture gradient refractive index lens for two-photon fluorescence endoscopy. i, 37(11): 2001-2003, 2012. https://doi.org/10.1364/OL.37.002001.

[50] Wang Ch. and Ji N. Characterization and improvement of three-dimensional imaging performance of GRIN-lens-based two-photon fluorescence endomicroscopes with adaptive optics. *Optics Express*, 21(22): 27142-27154 (2013). https://doi.org/10.1364/OE.21.027142.

[51] Gosh, K.K., Burns, L.D., Cocker, E.D., Nimmerjahn, A., Ziv, Y., El Gamal, A. and Schnitzer, M.J. Miniaturized integration of a fluorescence microscope. *Nature Methods,* 8(10): 871-878, 2011. https://doi.org/ doi:10.1038/nmeth.1694.

[52] Göbel, W., Kerr, J.N., Nimmerjahn, A. and Helmchen, F. Miniaturized two-photon microscope based on a flexible coherent fiber bundle and a gradient-index lens objective. *Optics letters*, 29(21): 2521 - 2523, 2004. https://doi.org/10.1364/OL.29.002521.

[53] Hoy, C. L., Durr, N.J., Chen, P., Piyawattanametha, W., Ra, H., Solgaard, O. and Ben-Yakar, A.. Miniaturized probe for femtosecond laser microsurgery and two-photon imaging. *Optics Express*, 16(13): 9996-10005, 2008. https://doi.org/10.1364/OE.16.009996.

[54] Flusberg, B.A., Nimmerjahn, A., Cocker, E.D., Mukamel, E.A., Barretto, R.P.J., Jung, J.C. and Schnitzer, M.J. High-speed, miniaturized fluorescence microscopy in freely moving mice. *Nature Methods*, 5(11): 935-938, 2008. https://doi.org/10.1038/nmeth.1256.

[55] Barretto, R.P.J., Ko, T.H., Jung, J.C., Wang, T.J., Capps, G., Waters, A.C., Ziv, Y., Attardo, A., Recht, L. and Schnitzer, M.J. Time-lapse imaging of disease progression in deep brain areas using fluorescence microendoscopy. *Nature Medicine*, 17(2): 223-228, 2011. https://doi.org/10.1038/nm.2292.

[56] Mekhail, S.P., Arbuthnott, G., and Chormaic, S.N. Advances in Fibre Microendoscopy for Neuronal Imaging. *Optical Data Processing and Storage*, 2:30-42, 2016. https://doi.org/10.1515/odps-2016-0003.

[57] Delaney, P. and Martin Harris, M. Fiber-Optics in Scanning Optical Microscopy. In *Handbook of Biological Confocal Microscopy*, pages 508–515. Springer US, New York, USA, Third edition, 2006.

[58] Ozbay, B.N., Losacco, J.T., Cormack, R., Weir, R., Bright, V.M., Gopinath, J.T., Restrepo, D. and Gibson, E.A. Miniaturized fiber-coupled confocal fluorescence microscope with an electrowetting variable focus

lens using no moving parts. *Optics Letters,* 40(11): 2553-2556, 2015. https://doi.org/10.1364/OL.40.002553.

[59] Engelbrecht, C.J., Voigt, F. and Helmchen, F. Miniaturized selective plane illumination microscopy for high-contrast *in vivo* fluorescence imaging. *Optics Letters,* 35(9): 1413-1415, 2010. https://doi.org/10.1364/OL.35.001413.

[60] Laemmel, E., Genet, M., Le Goualher, G., Perchant, A., Le Gargasson, J.-F. and Vicaut, E. Fibered Confocal Fluorescence Microscopy (Cell-viZio™) Facilitates Extended Imaging in the Field of Microcirculation. *Journal of Vascular Research*, 41(5): 400-411, 2004. https://doi.org/10.1159/000081209.

[61] Čižmár, T. and Dholakia, K. Exploiting multimode waveguides for pure fibre-based imaging. *Nature Communication*, 3: 1027, 2012. https://doi.org/10.1038/ncomms2024.

[62] Papadopoulos, I.N., Farahi, S., Moser, C. and Psaltis, D. High-resolution, lensless endoscope based on digital scanning through a multimode optical fiber. *Biomedical Optics Express*, 4(2): 260–270, 2013. https://doi.org/10.1364/BOE.4.000260.

[63] Szabo, V., Ventalon, C., De Sars, V., Bradley, J. and Emiliani, V. Spatially selective holographic photoactivation and functional fluorescence imaging in freely behaving mice with a fiberscope. *Neuron*, 84(6): 1157-69, 2014. https://doi.org/10.1016/j.neuron.2014.11.005.

[64] Xu, H.T., Pan, F., Yang, G. and Gan, W.B. Choice of cranial window type for in vivo imaging affects dendritic spine turnover in the cortex. *Nature Neuroscience,* 10(5): 549-51, 2007. https://doi.org/10.1038/nn1883.

[65] Moshayedi, P., Ng, G., Kwok, J.C.F., Yeo, G.S.H., Bryant, C.E., Fawcett, J.W., Franze, K. and Guck, J. The relationship between glial cell mechanosensitivity and foreign body reactions in the central nervous system. *Biomaterials*, 35(13): 3919-25, 2014. https://doi.org/10.1016/j.biomaterials.2014.01.038.

[66] Eguchi, M. and Horinouchi, S. Finite-element modal analysis of large-core multimode optical fibers. *Applied Optics,* 43(10): 2163-2167, 2004. https://doi.org/10.1364/AO.43.002163.

[67] Čižmár, T., Mazilu, M. and Dholakia, K. In situ wavefront correction and its application to micromanipulation. *Nature Photonics*, 4: 388-394, 2010. https://doi.org/10.1038/nphoton.2010.85.

[68] Čižmár, T., Dholakia, K. Shaping the light transmission through a multimode optical fibre: complex transformation analysis and applications in biophotonics. *Optics Express*, 19(20): 18871-18884, 2011. https://doi.org/10.1364/OE.19.018871.

[69] Mahalati, R.N., Gu, R.Y. and Kahn, J.M. Resolution limits for imaging through multi-mode fiber. *Optics Express,* 21(2): 1656-1668, 2013. https://doi.org/10.1364/OE.21.001656.

[70] Plöschner, M., Tyc, T. and Čižmár, T. Seeing through chaos in multimode fibres. *Nature Photonics,* 9:529-535, 2015. https://doi.org/10.1038/nphoton.2015.112.

[71] Turtaev, S., Leite, I.T., Altwegg-Boussac, T., Pakan, J.M.P., Rochefort, N.L. and Čižmár, T. High-fidelity multimode fibre-based endoscopy for deep-brain *in vivo* imaging. *Light: Science and Applications*, 7:92, 2018. https://doi.org/10.1038/s41377-018-0094-x.

[72] Wadsworth, W., Percival, R., Bouwmans, G., Knight, J., Birks, T., Hedley, and P. S. Russell, P.S., "Very high numerical aperture fibers," *Photonics Technology Letters,* 16: 843–845, 2004. https://doi.org/10.1109/LPT.2004.823689.

[73] Mosk, A.P., Lagendijk, A., Lerosey, G., and Fink, M. Controlling waves in space and time for imaging and focusing in complex media. *Nature Photonics*, 6: 283-292, 2012. https://doi.org/10.1038/nphoton.2012.88.

[74] Vellekoop, I.M. & Mosk, A. Universal Optimal Transmission of Light Through Disordered Materials. *Physical Review Letters*, 101:120601 2008. https://doi.org/10.1103/PhysRevLett.101.120601.

[75] Popoff, S., Lerosey, G., Fink, M., Boccara, A.C. and Gigan, S. Image transmission through an opaque material. *Nature Communications* 1(81), 2010. https://doi.org/10.1038/ncomms1078.

[76] Vellekoop, I.M. and Mosk, A. Focusing coherent light through opaque strongly scattering media. *Optics Letters*, 32(16): 2309–2311, 2007. https://doi.org/10.1364/OL.32.002309.

[77] Conkey, D.B., Brown, A.N., Caravaca-Aguirre, A.M. and Piestun, R. Genetic algorithm optimization for focusing through turbid media in noisy environments. *Optics Express,* 20(5): 4840–4849, 2012. https://doi.org/10.1364/OE.20.004840.

[78] Popoff, S.M., Aubry, A., Lerosey, G., Fink, M., Boccara, A.C. and Gigan, S. Exploiting the Time-Reversal Operator for Adaptive Optics, Selective Focusing, and Scattering Pattern Analysis. *Physical Review Letters*, 107(26): 263901, 2011. https://doi.org/10.1103/PhysRevLett.107.263901.

[79] Mounaix, M., Fontaine, N.K., Neilson, D.T. and Carpenter, J. Time reversal of optical waves. Frontier in Optics+Laser Science APS/DLS, 2019. https://doi.org/10.1364/FIO.2019.FTu6B.5.

[80] Papadopoulos, I.N., Farahi, S., Moser, C. and Psaltis, D. Focusing and scanning light through a multimode optical fiber using digital phase conjugation. *Optics Express,* 20(10): 10583–10590, 2012. https://doi.org/10.1364/OE.20.010583.

[81] Drémeau, A., Liutkus, A., Martina, D., Katz, O., Schülke, C., Krzakala, F., Gigan, S._ and Daudet, L. Reference-less measurement of the transmission matrix of a highly scattering material using a DMD and phase retrieval techniques. *Optics Express,* 23(9). 11898-1911, 2015. https://doi.org/10.1364/OE.23.011898.

[82] Popoff, S.M., Lerosey, G., Carminati, R., Fink, M., Boccara, A.C. and Gigna, S. Measuring the transmission Matrix in Optics: An Approach to the Study and Control of Light Propagation in disordered Media. *Physical Review Letters,* 104(10): 100601 2010. https://doi.org/10.1103/PhysRevLett.104.100601.

[83] Vasquez-Lopez, S. A., Koren, V., Plöschner, M., Padamsey, Z., Čižmár, T. and Emptage, N. J. Minimally invasive deep-brain imaging through a 50 μm-core multimode fibre. *bioRxiv,* 2018. https://doi.org/10.1101/289793.

[84] Ohayon, S., Caravaca-Aguirre, A., Piestun, R. and DiCarlo, J.J. Minimally invasive multimode optical fiber microendoscope for deep brain fluorescence imaging. Biomedical *Optics Express,* 9(4): 1492-1509, 2018. https://doi.org/10.1364/BOE.9.001492.[85] Thorlabs, Inc.

[86] Leite, I. T., Turtaev, S., Jiang, X., Šiler, M., Cuschieri, A., Russell, P. St. J. and Tomáš Čižmár. Three-dimensional holographic optical manipulation through a high-numerical-aperture soft-glass multimode fibre. *Nature Photonics,* 12(7): 33-39, 2017. https://doi.org/10.1038/s41566-017-0053-8.

[87] Turtaev, S. Leite, I.T., Mitchell, K.J., Padgett, M.J., Phillips, D.B. and Čižmár T. Comparison of nematic liquid-crystal and DMD based spatial light modulation in complex photonics. *Optics Express,* 25(24): 29874-29884, 2017. https://doi.org/10.1364/OE.25.029874.

[88] Sampsell J.B. Digital micromirror device and its application to projection displays. *Journal of Vacuum Science and Technology B,* 12,3242 1994. https://doi.org/10.1116/1.587506.

[89] Nesbitt R.S., Smith S.L., Molnar R.A. and Benton S.A., Holographic recording using a digital micromirror device, *SPIE*, 3637, 1999. https://doi.org/10.1117/12.343767.

[90] Kreis T., Aswendt P., Hoefling, R. Hologram reconstruction using a digital micromirror device. *Society of Photo-Optical Instrumentation Engineers,* 40(6): 926-933, 2001. https://doi.org/10.1117/1.1367346.

[91] Leonardo, R.D. and Bianchi, S. Hologram transmission through multi-mode optical fibers. *Optics Express,* 19(1): 247–254, 2011. https://doi.org/10.1364/OE.19.000247.

[92] Dudley D., Duncan W. and Slaughter J. Emerging Digital Micromirror Device (DMD) Applications, SPIE, 4985, 2003. 10.1117/12.480761.

[93] Gomez, A.D., Turtaev, S., Du, Y. and Čižmár, T. Near perfect focusing through multimode fibres, *Optics Express,* 30(7): 10645-10663, 2022. https://doi.org/10.1364/OE.452145.

[94] Phillips, D.B., Sun, M-J., Taylor, J.M., Edgar, M-P, Barnett, S.M., Gibson, G.G. and Padgett, M.J. Adaptive foveated single-pixel imaging with dynamic super-sampling.arXiv:1607.08236,2016. https://doi.org/10.48550/arXiv.1607.08236.

[95] Mitchell, K.J., Turtaev, S., Padgett, M.J., Čižmár, T. and Phillips, D.B. High-speed spatial control of the intensity, phase and polarization of vector beams using a digital micro-mirror device. *Optics Express,* 24(25): 29269-29282, 2016. https://doi.org/10.1364/OE.24.029269.

[96] Bianchi, S. and Di Leonardo, R. A multi-mode fiber probe for holographic micromanipulation and microscopy. *Lab on a Chip,* 12: 635–639, 2012. https://doi.org/10.1039/C1LC20719A.

[97] Rudolf, B., Du, Y., Turtaev, S., Leite, I.T. and Čižmár T. Thermal stability of wavefront shaping using a DMD as a spatial light modulator. *Optics Express,* 29(25): 41808-41818, 2021. https://doi.org/10.1364/OE.442284.

[98] Bertero, M., Boccacci, P., Desiderà, G. and Vicidomini, G. Image deblurring with poisson data: from cells to galaxies. Inverse Problems, 25(12): 123006, 2009. http://iopscience.iop.org/0266-5611/25/12/123006.

[99] Karl,W. "3.6 - regularization in image restoration and reconstruction," in *Handbook of Image and Video Processing (Second Edition),* A. Bovik, ed. (Academic, 2005), Communications, Networking and Multimedia, pp. 183 – V, 2nd.ed.

[100] Wang, Z., Bovik, A., Sheikh, H. and Simoncelli, E. Image quality assessment: from error visibility to structural similarity. *IEEE Transactions on Image Processing*, 13(4): 600–612, 2004. https://doi.org/10.1109/TIP.2003.819861.

[101] Makitalo, M. and Foi, A. Optimal inversion of the ascombe transformation in low-count poisson image denoising. *IEEE Transactions on Image Processing*, 20(1): 99–109, 2011. https://doi.org/10.1109/TIP.2010.2056693.

[102] Yu, Y.-C., Bultje, R.S., Wang, X. and Shi, S.-H.Specific synapses develop preferentially among sister excitatory neurons in the neocortex. Nature Letters, 458(7237): 501-504, 2009. https://doi.org/10.1038/nature07722.

[103] Mateo, C., Avermann, M., Gentet, L.J., Zhang, F., Deisseroth, K. and Petersen, C.C.H. In Vivo Optogenetic Stimulation of Neocortical Excitatory Neurons Drives Brain-State-Dependent Inhibition. *Current Biology*, 21(19): 1593-602, 2011. https://doi.org/ 10.1016/j.cub.2011.08.028.

[104] Miller, S.M. and Sahay, A. Functions of adult-born neurons in hippocampal memory interference and indexing. Nature Neuroscience, 22: 1565-1575, 2019. https://doi.org/10.1038/s41593-019-0484-2.

[105] Leite I., Turtaev, S., Boonzajer Flaes, D.E. and Čižmár, T. Observing distant object with a multimode fiber-based holographic endoscope. *APL Photonics*, 6, 036112, 2021. https://doi.org/10.1063/5.0038367.

[106] Silveira, B.M., Pikálek, T., Stibůrek, M., Ondráčková, P., Jákl, P., Leite, I.T. and Čižmár, T. Side-view holographic endomicroscopy via a custom-terminated multimode fibre. *Optics Express*, 29(15):23083-23095, 2021. https://doi.org/10.1364/OE.426235.

[107] Stibůrek, M., Ondráčková, P., Tučková, T., Turtaev, S., Šiler, M., Pikálek, T., Jákl, P., Gomes, A., Krejčí, J., Kolbábková, P., Uhlířová, H. and Čižmár, T. Hair-thin endo-microscope for deep-brain in-vivo observations of neuronal connectivity, activity and blood flow dynamics. *Submitted* 2022.

Appendix A

Step	Temperature [°C]	Time [min]	Cycles
Initial Denaturation	94	3	1
Denaturation	94	1	10
Annealing	65 (-0.5 per cycle)	1	
Extension	72	2	
Denaturation	94	1	28
Annealing	60	1	
Extension	72	2	
Final Extension	72	10	1
Final Hold	4	$10 \leq \infty$	

Table 3.1: PCR protocol for DNA amplification.

Name	Composition	Supplier
REDExtract-N-Amp PCR Reaction Mix	buffer, salts, dNTPs, Taq polymerase	Sigma-Aldrich
REDExtract-N-Amp™ Tissue PCR Kit	Extraction Solution, Tissue Preparation Solution, Neutralization Solution	Sigma-Aldrich
Primer F tdTomato - oIMR9105	oligonucleotides	Generi Biotech
Primer R tdTomato - oIMR9103	oligonucleotides	Generi Biotech
Primer F - 46549	oligonucleotides	Generi Biotech
Primer R - oIMR9074	oligonucleotides	Generi Biotech
10xTBE	1.0M TRIS-borat, pH 8.3, 20mM EDTA	P-Lab
SYBER	SYBER™ Safe nucleic acid del stain red	Thermo Fisher Scientific
ROTI® Load DNA	Tris, Na-acetate, EDTA, bromophenol blue, xylene cyanol, glycerol	Carl Roth
Isoflurane	Isofluranum 1000mg/g	Vetpharam animal health, s.l.
Ketamine	Narkamon 50 mg/ml	bioveta
Xylazine - Xylazine Ecuphar	Xylazinum 20 mg/ml	Alverta werfft, Ecuphar N.V.
PBS	Dulbecco´s Phosphate Buffered Saline, without Ca and Mg, 20 ml	Lonza, 17-512Q
PFA	Paraformaldehyde	Sigma-Aldrich

Table 3.2: List of chemical solutions used during preparation of fixed brain slices.